



Activation energy for pore opening in lipid membranes under an electric field

Eulalie J. Lafarge^a , Pierre Muller^a , André P. Schroder^b, Ekaterina Zaitseva^{c,d}, Jan C. Behrends^c, and Carlos M. Marques^{a,e,1}

Edited by David Weitz, Harvard University, Cambridge, MA; received August 1, 2022; accepted February 4, 2023

The standard model of pore formation was introduced more than fifty years ago, and it has been since, despite some refinements, the cornerstone for interpreting experiments related to pores in membranes. A central prediction of the model concerning pore opening under an electric field is that the activation barrier for pore formation is lowered proportionally to the square of the electric potential. However, this has only been scarcely and inconclusively confronted to experiments. In this paper, we study the electropermeability of model lipid membranes composed of 1-palmitoyl-2-oleyl-glycero-3-phosphocholine (POPC) containing different fractions of POPC-OOH, the hydroperoxidized form of POPC, in the range 0 to 100 mol %. By measuring ion currents across a 50-μm-diameter black lipid membrane (BLM) with picoampere and millisecond resolution, we detect hydroperoxidation-induced changes to the intrinsic bilayer electropermeability and to the probability of opening angstrom-size or larger pores. Our results over the full range of lipid compositions show that the energy barrier to pore formation is lowered linearly by the absolute value of the electric field, in contradiction with the predictions of the standard model.

electroporation | pore formation | electropermeability | lipid hydroperoxidation

Membrane electroporation, the opening of pores in biomembranes under electric fields, has nowadays become a well-established technique in medicine, food processing, and biotechnology to permeabilize the membrane of cells, thus allowing delivery of drugs and other molecules (1). Despite its clear importance, the physical origin of pore opening by electrical fields is intensely debated, and, in defiance of long-standing theoretical and numerical simulation efforts, no unified and quantitative view of the phenomenon has yet emerged. Crucially, the most developed theoretical model for pore opening usually referred to as the standard model of pore formation has never been validated or seriously challenged by experimental data, mainly due to the scarcity of experimental efforts designed to test the main predictions of the model (2). This jeopardizes progress in the field, particularly when one considers that every aspect of the widespread phenomenology that relates to lipid membranes with pores refers to or stands on the framework provided by the standard model. In particular, the standard model assumes that pore nucleation under an electric field is a direct consequence of membrane tension changes; since there is evidence that tension depends quadratically on the electric field (3), the model predicts a quadratic decrease of the activation barrier of pore formation with V , the electric potential jump across the membrane—please see the table in *Materials and Methods* for all quantities and their units. Results from numerical simulations do provide a molecular view of the first steps of pore formation but have only very rarely been compared to experiments or developed to a point where an operational model of pore formation can be elaborated (4). In this paper, we test the predicted V^2 reduction of the activation barrier of pore formation in lipid membranes assembled from mixtures of POPC and its hydroperoxidized form POPC-OOH.

Lipid oxidation, a natural outcome of metabolic activity under oxygen, impacts the structure and functioning of biomembranes. While a moderate and controlled amount of oxidation is required for signaling and other cell mechanisms, imbalanced generation of oxidized lipid species has been linked to several diseases such as atherosclerosis, diabetes, Parkinson, and Alzheimer and is known to play a role in aging and carcinogenesis (5). In medicine, photodynamic therapy (PDT) removes undesirable tissue through light-induced oxidation as an alternative to surgery. Although oxidation of lipids can be due to several causes and results in a variety of final chemical transformations, the first step is always the insertion of a dioxygen at the site of an unsaturated bond, resulting in a hydroperoxidized lipid form (6), such as those displayed in Fig. 1. Somewhat unexpectedly, it was found that bilayers can be assembled from fully hydroperoxidized

Significance

Why does a pore open when a high-enough electric field is applied to a lipid bilayer? Scarcity of data from experiments designed to probe this important phenomenon has so far precluded a clear answer to the question. Here, we report results from electropermeation experiments on black lipid membranes assembled from different mixtures of a common lipid, 1-palmitoyl-2-oleyl-glycero-3-phosphocholine (POPC), and its hydroperoxidized form POPC-OOH. By carefully identifying pore formation events, we were able to quantify the influence of the applied electric field and of the hydroperoxidation degree on the frequency of pore opening. Our results disagree with the standard model of pore formation and bring a significant insight into the factors controlling pore opening under an electric field.

Competing interest statement: The authors have organizational affiliations to disclose. J.C.B. is co-founder of Nanion Technologies GmbH, Munich, Germany. J.C.B. and E.Z. are co-founders of Ionera Technologies GmbH, Freiburg, Germany. Yes, the authors have stock ownership to disclose. J.C.B. is shareholder of Nanion Technologies GmbH, Munich, Germany. J.C.B. and E.Z. are shareholders of Ionera Technologies GmbH, Freiburg, Germany.

This article is a PNAS Direct Submission.

Copyright © 2023 the Author(s). Published by PNAS. This article is distributed under Creative Commons Attribution-NonCommercial-NoDerivatives License 4.0 (CC BY-NC-ND).

¹To whom correspondence may be addressed. Email: carlos.marques@ens-lyon.fr.

This article contains supporting information online at <http://www.pnas.org/lookup/suppl/doi:10.1073/pnas.2213112120/-DCSupplemental>.

Published March 7, 2023.

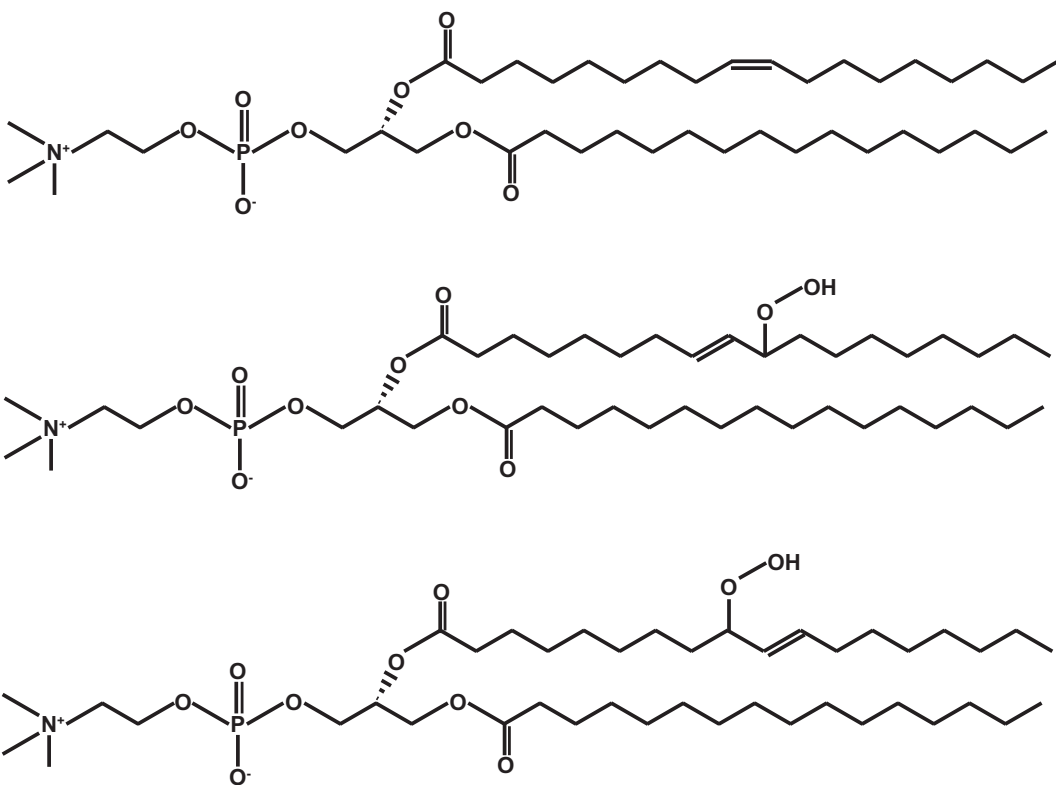


Fig. 1. POPC and POPC-OOH isomers.

lipids, at least for POPC-OOH, which bears one hydroperoxide group per lipid, and for DOPC-OOH₂, the hydroperoxidized form of 1, 2-dioleoyl-glycero-3-phosphocholine (DOPC), which bears two OOH groups, i.e., one per chain (7). This allowed to better probe the nature of hydroperoxidized lipid bilayers for which much structural information was obtained: Hydroperoxidation significantly increases the area per lipid ($\sim 15\%$ for POPC-OOH and $\sim 20\%$ for DOPC-OOH₂) with a concomitant reduction of bilayer thickness; it also weakens the stretching modulus of the bilayers, reducing it for both DOPC and POPC from circa 200 mN·m⁻¹ to 50 mN·m⁻¹ (7). These and other measured properties such as membrane polarity and viscosity (8) reinforce suggestions from computer simulations (9, 10) and from X-ray scattering data (11) that the preferential migration to the interface between water and the hydrophobic core of a fraction or of all the hydroperoxide groups is the main driving factor of structural membrane modifications. Given the extent of such conformational changes, it came as a surprise that bilayers from pure POPC-OOH or DOPC-OOH₂ preserve their impermeability to sugars at least over several hours—the typical duration of experiments with giant unilamellar vesicles (GUVs) (7). This brings into question the ability of hydroperoxidized lipid bilayers to maintain gradients of other biorelevant small particles such as ions (12).

Biomembranes allow water molecules to cross their $\ell \sim 5$ -nm-thick barrier with permeability coefficients P_m as high as $P_m \sim 10^{-5}$ m·s⁻¹ while being almost impermeable to the majority of hydrophilic solutes (13). For charged species, permeability is many orders of magnitude smaller at 10^{-12} m·s⁻¹ for Cl⁻ and 10^{-14} m·s⁻¹ for K⁺, two common biorelevant ions (14). Permeability values for water and other molecules can

be rationalized within a simple picture where a molecule driven by a chemical potential gradient climbs the membrane barrier of free-energy height U_m with probability $\sim \exp(-U_m/k_B T)$, where k_B is the Boltzmann constant and T the absolute temperature, and moves over the barrier top with velocity D/ℓ , thus leading to $P_m = (D/\ell) \exp(-U_m/k_B T)$. With typical diffusion coefficients in oil $D \sim 10^{-9}$ m²·s⁻¹, a molecule takes a few tens of nanoseconds to cross the barrier once it has climbed it (13). For water, the partition coefficient $K_w = \exp(-U_m/k_B T)$, measured often between water and hexadecane, is given by $K_w \sim 10^{-5}$ (barrier U_m of order of ten $k_B T$), with correspondingly much smaller values for ions, $K_{Cl^-} \sim 10^{-12}$ and $K_{K^+} \sim 10^{-14}$ (and barriers \sim three times larger than for water). As a practical consequence, charge gradients can be indefinitely maintained across lipid membranes, even for large cell-sized lipid vesicles of $R \sim 10$ μ m radius that can equilibrate an osmotic imbalance of $\Delta C \sim 20$ mM within a thousand seconds ($\tau_w \sim R/(P_m v_w \Delta C) \sim 1000$ s), with v_w being the water molar volume.

In our quest to understand charge transport across lipid membranes, we performed experiments in a BLM geometry—*SI Appendix*, Fig. S1, carefully identifying and quantifying charge transport events and determining ionic permeabilities in membranes assembled from POPC/POPC-OOH mixtures in a solution of 100 mM KCl. For all bilayers, we witnessed the emergence of angstrom-size single pore opening as the field strength was increased, thus allowing to quantify the influence of the field strength on the probability of initial pore formation. Our results do not only bring an extensive set of data to the field of electroporation but also challenge some of the prevailing views in the field.

Results

Our experiments focus on the analysis of the ionic current crossing phospholipid membranes composed of various mole fractions (X_{OOH}) of POPC-OOH. In the following, we will first describe and characterize conduction events as a function of applied voltage and hydroperoxidation degree and determine membrane ability to withstand the electric field without rupturing. We then perform a quantitative analysis of intrinsic (pore-free) electropermeability. Finally, we quantify the membrane propensity to open pores as a function of applied voltage, identifying the opening of single pores and studying their characteristic lifetimes, intensities, and frequency of formation.

Traces of Electric Current. In our experiments, the information on charge transport is contained in the time series of the measured current $I(t)$ for a given applied voltage; *SI Appendix*, Fig. S2 for our voltage ramping protocol and *SI Appendix*, Fig. S3 for the equivalent electric circuit. Given the typical values for the membrane capacitance in the picofarad range—*SI Appendix*, Fig. S4 for measured values—and the series resistance of order of a few tenths of a megaohm, the response time of the equivalent electric circuit is a few microseconds; *SI Appendix*, sections S3 and S4. Thus, relaxation phenomenon in our traces, associated,

for instance, with the decay time τ of the capacitance peaks and current increase after pore opening, is a result of the filtering process implemented in the recording apparatus and in the software, typically on the order of a few milliseconds, $\tau \simeq 2.7$ ms; *SI Appendix*, Fig. S5 for filtering and *SI Appendix*, Fig. S6 for chosen examples of current traces.

Fig. 2 proposes a classification of conductance events based on the shape of the observed current fluctuation and assigns each class to a hypothetical mechanism on the level of membrane structure and dynamics. The average current that we designate as I_c is present in all traces. In the absence of an applied voltage V , one has $I_c = 0$; the membrane simply separates two volumes of the ionic solution. When a voltage V is applied, the membrane acts as a capacitor of a few picofarad with a “leakage” current I_c of order of several picoamperes. The lipid bilayer bears thus, under an applied potential of 100 mV, roughly one charge per $\simeq 200$ nm 2 corresponding to 350 lipids. The same area also lets one charge per second cross the membrane barrier.

Fig. 2, *iii* and *iv* show current fluctuations when a large-enough V induces a sudden rise of the current above its baseline value I_c , reaching a maximum and then immediately—case (*iii*)—or after a plateau phase—case (*iv*)—returning to the baseline. This is the signature of pore opening, the number of charges conveyed through a pore being a function of the applied voltage, of the ion

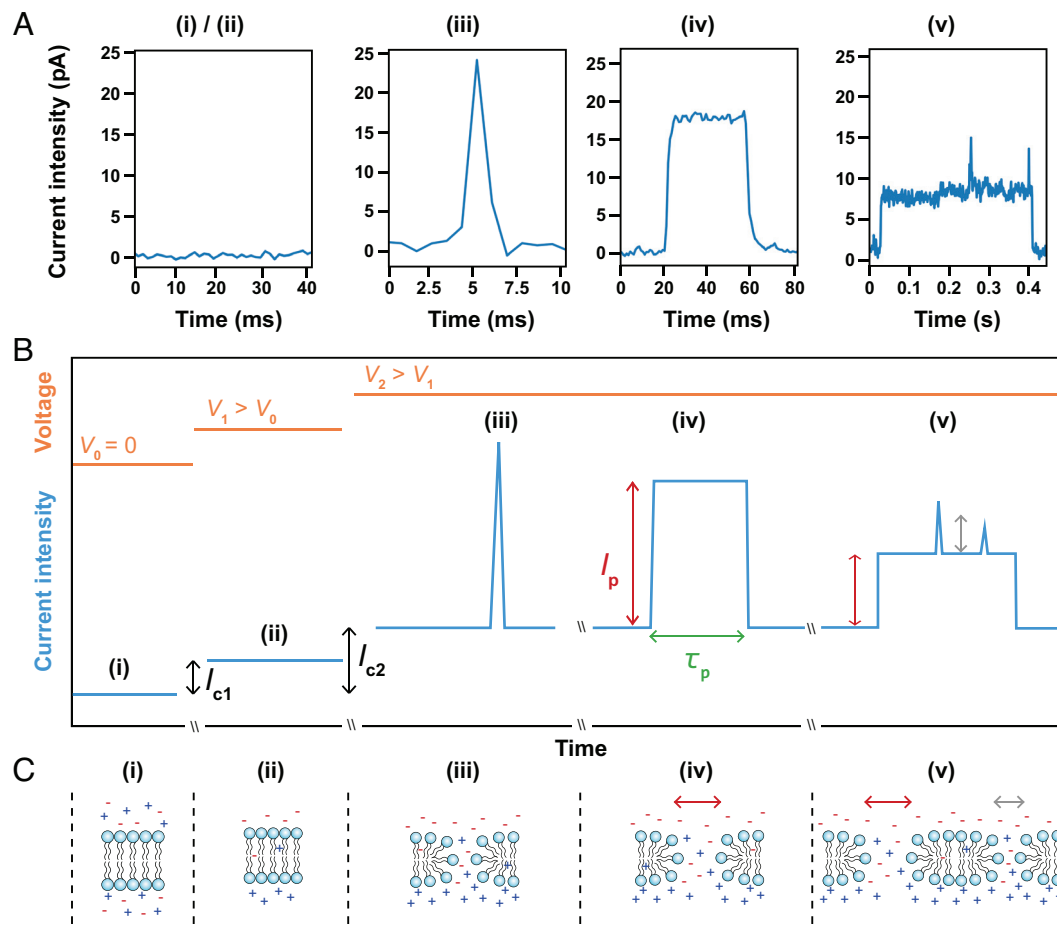


Fig. 2. Current traces and associated membrane geometry. (A) Identifiable segments of $I(t)$ along with (B) their schematic representation and (C) their presumed membrane conformation. Under no (*i*) or small (*ii*) applied voltages, the current fluctuates smoothly about a small (\sim pA) average current. Charges accumulate on both sides of the membrane that acts as a capacitor; a small amount of ions cross the membrane. Under larger applied voltages, the opening of short lifetime pores (*iii*) and long lifetime pores (*iv*) can be detected by the sudden rise of the current. Pores can accommodate lipid heads along the pore rim, in a conformation referred to as hydrophilic pores. Small numbers of simultaneous pores still allow for identifiable membrane geometries (*v*).

concentration in the solution and, importantly for the interpretation of the results, of the pore size. Under our conditions, for an applied voltage of 100 mV, a simple conduction model (15) predicts that a pore of $D_p = 1$ -nm diameter generates a stationary current I_p of 20 pA with intensity values I_p for pores of different sizes scaling as $I_p \propto D_p^2$. Since pore opening and closing is much faster than the characteristic instrument response time τ , model variations for pore opening can be taken as square gate functions for $D_p(t)$ such as $D_p(t) = D_p$ for $t_i < t < t_i + \tau_p$ and $D_p(t) = 0$ otherwise, with t_i and τ_p being the pore initial time and lifetime, respectively; *SI Appendix, Fig. S4*. (iii) shows an example of a short pore, *i.e.*, $\tau_p < \tau$, while (iv) shows the opposite example of a long-lived pore where $\tau_p \gg \tau$ and thus a stationary plateau can be reached before the pore closes; *SI Appendix, section S3*. Fig. 2, v shows a more complex signal where individual events are nevertheless still *identifiable*. We name trace segments *complex* when the state of the membrane cannot be inferred from the current traces.

Membrane Rupture Under an Applied Voltage. As explained before, experiments were performed by ramping up V as shown in *SI Appendix, Fig. S2*. Voltage values at which membrane breakage occurred were collected and averaged to build the membrane survival probability under an imposed voltage—*SI Appendix, Fig. S12*. While pure POPC membranes (0% -OOH) have a 50% probability of breaking at 300 mV in a time span of 6 s, both for positive and negative applied voltages, for nearly fully hydroperoxidized membranes (96% -OOH), the 50% rupture probability is reached at 175 mV. Hydroperoxidation, as we will below quantify for all investigated phenomena, renders the membranes increasingly vulnerable to electric fields.

Membrane Intrinsic Conductivity. If one pictures the lipid membrane as a one-dimensional (1D) barrier restricting ionic mobility in the direction perpendicular to the bilayer, the standard formulations by Goldman et al. (13, 14, 16, 17) can be used to predict the ion current density $i_c = I_c/S$, where S is the effective membrane area contributing to the electric measurement (that we infer from the measured capacity), and I_c is the current measured on *all trace sections devoid of pores*. A simple step-like potential that depends only on the barrier height U_m and on the barrier thickness ℓ leads to a linear relationship between the current and the applied potential. Current–voltage relations $i_c(V)$ with a supralinear component can be obtained from barrier functions of a more complex shape. The simpler of these is the trapezoidal barrier, where the basis of the barrier has thickness ℓ , while the top of the barrier at height U_m is thinner, with thickness $b \leq \ell$ (18). Conductivity predictions from the trapezoidal barrier can be written as a cubic expansion of the applied potential:

$$i_c = e c P_m u \left(1 + \left(1 - \frac{b^2}{\ell^2} \right) \frac{u^2}{24} \right), \quad [1]$$

with $u = eV/(k_B T)$, e the elementary charge, and c the ion concentration.

Fig. 3A presents $i_c(V)$ data and fitted curves for all the hydroperoxidation degrees. Results are plotted as a function of both the normalized voltage u and the actual voltage V . For better comparison with results from the literature, we provide two Y-axis scales, for both the measured current density (left) and the current crossing a membrane with 42-μm diameter, the average diameter of our membranes as inferred above from capacity measurements.

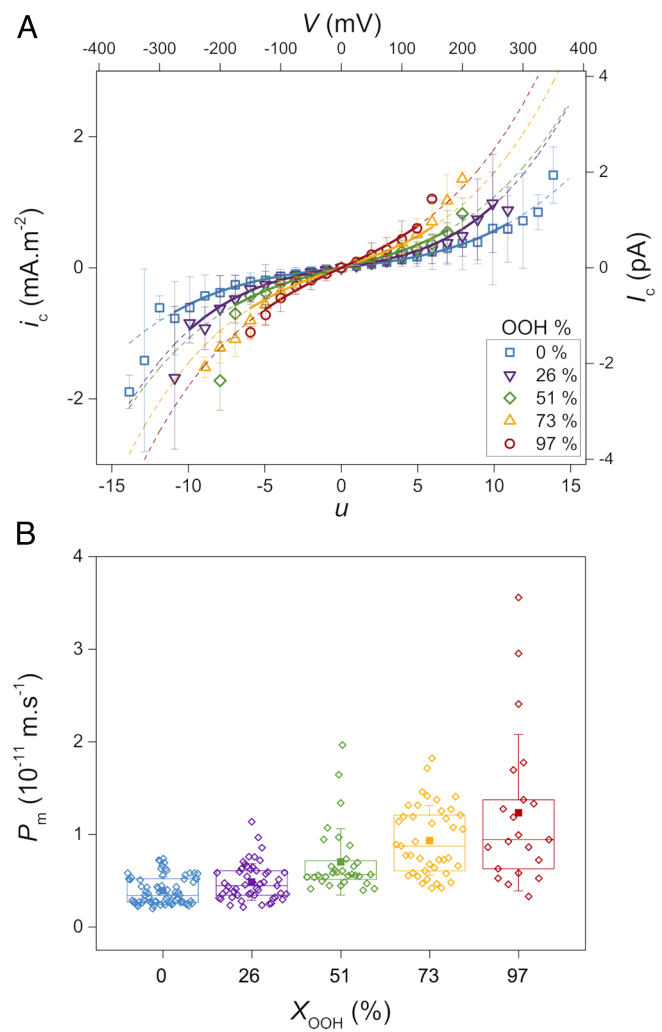


Fig. 3. Intrinsic membrane electroporability. (A) $i_c - V$ characteristics in a pore-free membrane. The left axis measures current density, and the right axis expresses current across a patch of 42-μm diameter. The X-axis displays normalized voltage units $u = eV/(k_B T)$; voltage is shown in the top horizontal axis. Full lines drawn in the range where Eq. 1 adequately fits the data; dashed lines extrapolate the fit over the whole range as a guide to the eyes; error bars measure the SD. (B) Permeability of POPC membranes as a function of X_{OOH} , the molar fraction of hydroperoxidized lipids. The data are displayed as box-plots representing the distribution of membrane permeability based on the first quartile, median, mean (filled square symbol), and third quartile, with whiskers showing SD.

Eq. 1 fits well the data over a voltage range (shown by full lines in the figure) that depends on the peroxidation degree but that is always large enough to allow for determination of the two fitting parameters, the permeability P_m and the ratio b/ℓ . P_m for pure POPC is measured at $2.8 \pm 2.5 \times 10^{-12}$ m·s⁻¹, consistent with reported permeability values for the anion Cl⁻ that dominates charge transport across the lipid membrane (14). Values of P_m increase steadily with the peroxidation level, as shown in Fig. 3B, up to $11 \pm 9 \times 10^{-12}$ m·s⁻¹ for the fully hydroperoxidized bilayer, an increase of roughly a factor 4 of the average values. Fittings return an almost constant value for the ratio $b/\ell = 0.87 \pm 0.05$, typical for values reported in the literature for lipid membranes (19). As stated above, membrane permeability is well described by $P_m = (\mathcal{D}/\ell) \exp(-U_m/k_B T)$. Observed changes of membrane permeability cannot be explained by the small decrease (~20%) of membrane thickness ℓ (11), and it is unlikely that the diffusion coefficient \mathcal{D} of the ions across

the membrane increases dramatically with hydroperoxidation, given the small volume fraction occupied by the added organic hydroperoxide. The observed increase is thus better interpreted as due to a lowering of the membrane barrier potential, $\Delta U_m = -1.4 k_B T$, at least with respect to anion Cl^- that dominates transport here, consistently with the known increase of polarity of the inner membrane region (20).

Pore Formation Correlates with Changes in the Barrier to Ions.

As V increases, the traces show the emergence of ionic transport across the membrane through pores, as depicted above in Fig. 2, *iii*, *iv*, and *v*.

We evaluate first the probability for a membrane to remain free of pores during the 6 s when a constant voltage is applied. Fig. 4 shows this probability for each membrane composition. As the figure shows, increasing X_{OOH} results, at any imposed voltage, in an increase of the probability for the membrane to create pores. For instance, hardly any pore can be detected for pure POPC membranes at applied voltages lower than 50 mV, while for the same voltage in half of the 96% POPC-OOH membranes, at least one pore was observed. Interestingly, the range of voltage over which Eq. 1 fits well data in Fig. 3*A* correlates with voltages at which pore opening probability reaches values higher than 0.90—*SI Appendix*, Fig. S13. Thus, the trapezoidal model behind Eq. 1 stops to be valid when the electric fields are high enough to bring the membrane to the verge of pore opening conditions.

Lifetime Distribution of Identifiable Pores. We developed a *threshold method*—*SI Appendix*, section S7—to detect identifiable pores with a well-defined opening and closing current jump. Using the results from this pore-detection routine, we built the distribution of pore lifetimes τ_p displayed in Fig. 5. Since no variation of pore lifetimes was observed with applied voltage (*SI Appendix*, Fig. S14), the results in Fig. 5 are computed by grouping all pores detected for a given -OOH composition irrespective of voltage.

The distribution of lifetimes is shown in Fig. 5 with 0.8-ms time bins. As the figure shows, there is no noticeable difference in the distributions for the various peroxidation degrees. If one excludes the first bin that is at the limit of time resolution, the

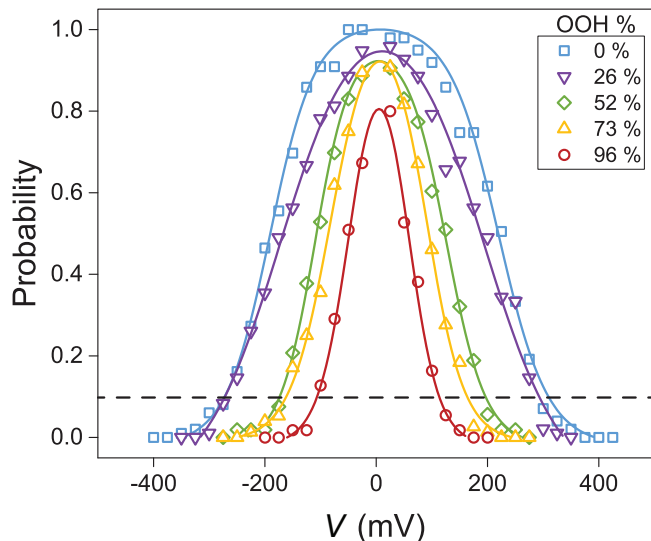


Fig. 4. Membrane probability to remain pore-free. Symbols represent the calculated probability; solid lines are a guide to the eyes. The dashed line indicates 10% probability.

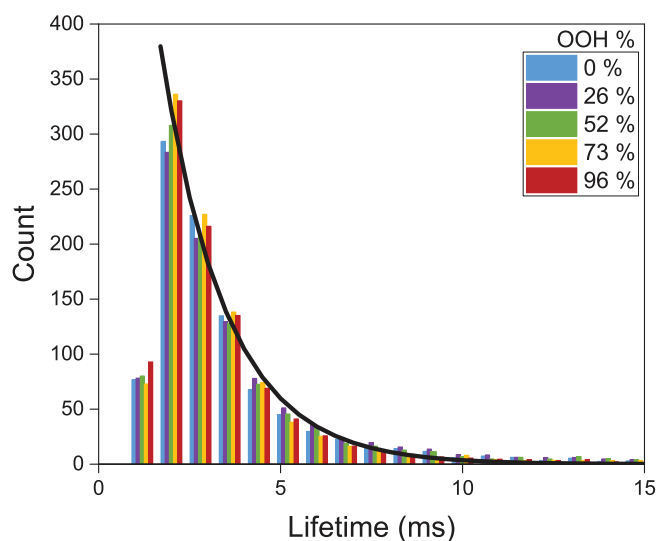


Fig. 5. Lifetime distribution of identifiable pores (bin = 0.8 ms) normalized for 1,000 pores. The solid line represents a single exponential fit.

combined distribution follows a single exponential decay with a time constant of 1.8 ± 0.1 ms (error computed from a 90% CI of the fit), similar to experiments recorded with 1-ms time resolution under BLM geometry in 100 mM KCl for diphyanoylphosphatidylcholine (DPhPC) membranes (21). It is remarkable that the lifetime is independent of X_{OOH} , suggesting that for these pores, lifetime is determined by phenomena extrinsic to the lipid bilayer. Indeed, as we recently showed (8), hydroperoxidation impacts both the chain and the head regions of the membrane, making it unlikely that intrinsic bilayers' contributions to the lifetime would be independent of hydroperoxidation degree. A relevant remark in this context is that at the pore site, the flow of charges creates an inhomogeneous electric field: The electrical potential difference across the membrane is strongly lowered close to the pore—it would vanish in the center of the pore for the case of a free flow of charges (22)—and it recovers far from the pore to its homogeneous value. Charge rearrangement must therefore take place laterally also, a process with a characteristic time that depends on the size of the region that is perturbed by the flow. This certainly calls for further modeling efforts of the electrical stresses acting on a membrane in the presence of pore flow.

In the following, we discriminate between short- and long-lived pores, as defined in *SI Appendix*, section S4, in order to better determine their characteristics and abundance.

Size of Short Lifetime Pores. Given the average lifetime of short-lived pores $\bar{\tau}_p = 1.8 \pm 0.1$ ms obtained by the *threshold method*, most of the pores detected in this category cannot reach a stationary conducting state which requires that the lifetime of the pore τ_p is larger than τ , the time needed to reach the stationary value I_p . It is nevertheless possible to obtain I_p values as explained in *SI Appendix*, section S3. Corresponding values of pores sizes can be computed (15) from $D_p = (4bI_p/\pi V\sigma)^{1/2}$ with $b = 5$ nm being the length of the pore and σ the solution conductivity, $\sigma = 1.29 \text{ S}\cdot\text{m}^{-1}$, for a 100 mM KCl solution (23). We obtained an average diameter $\bar{D}_p = 6.4 \pm 2.0 \text{ \AA}$ independently of applied voltage and hydroperoxidation degree, comparable to the lower range of reported radii (4, 21, 24, 25); *SI Appendix*, Fig. S16.

Opening Frequency of Short Lifetime Pores. We measure the frequency of detection of short lifetime pores using the *threshold method* mentioned above. Fig. 6 A shows the opening frequency of short lifetime pores expressed as the average number N_s of pore openings detected per second for a given applied voltage. As the figure shows, the frequency increases with both voltage and X_{OOH} .

The semilogarithmic representation of Fig. 6 A reveals a nearly linear dependence of $\ln N_s$ with applied voltage for all the samples, with an almost identical slope for all X_{OOH} . This suggests that under our conditions, frequency of pore opening follows the empirical relation:

$$N_s = f_p |u| \exp(\alpha |u|), \quad [2]$$

with all the information on X_{OOH} being carried by f_p alone. The master curve in Fig. 6 B was obtained by finding $f_p(X_{\text{OOH}})$ values that minimize vertical distance in the semilogarithmic representation of all curves with respect to $X_{\text{OOH}} = 0$. Fits of

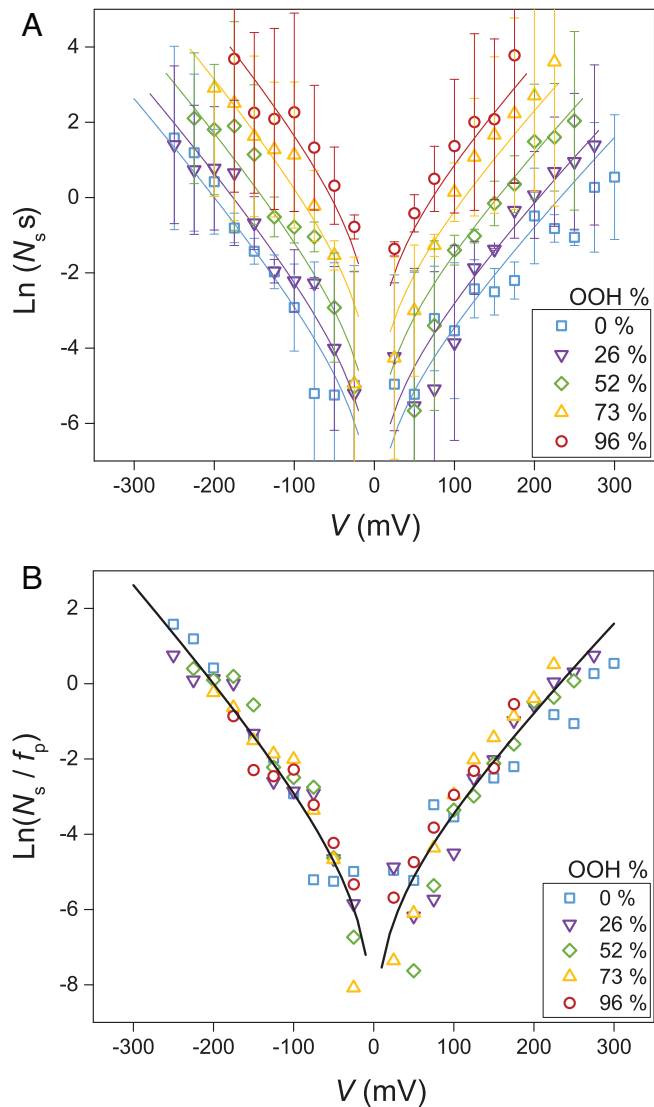


Fig. 6. (A) Average number of short lifetime pores opening per second as a function of voltage for the different hydroperoxidation degree of POPC membranes. Error bars represent SD. Solid lines represent fits by Eq. 2. (B) Master curve obtained by normalizing N_s over f_p . Please note that the Y-axis represents natural logarithm values.

this master plot give the pair of values ($\alpha^+ = 0.50 \pm 0.05$, $f_p^+(0) = 1.1 \pm 0.1 \times 10^{-3} \text{ s}^{-1}$) and ($\alpha^- = 0.56 \pm 0.06$, $f_p^-(0) = 1.5 \pm 0.1 \times 10^{-3} \text{ s}^{-1}$) for respectively the positive and the negative branches (errors from a 90% fit CI). *SI Appendix*, Fig. S19 displays the influence of X_{OOH} on the frequency f_p , which shows that both the positive and negative branches are well described by the function $\ln(f_p(X_{\text{OOH}})/f_p(0)) = -1.2 + 0.055X_{\text{OOH}}$ for all points except the first.

The number of short lifetime pores that we detect is a function of applied voltage and hydroperoxidation degree. The voltage dependence that we observe does not follow the predictions of the standard model for pore formation in lipid bilayers, nor those from the many variants of the model (2, 24, 26, 27). Central to those predictions is the dependence of the activation barrier for the pore creation rate with V^2 , the square of the applied potential. Incidentally, to our knowledge, this dependence has never been confirmed. Scarce data exist (21) that have been interpreted as a proof of such quadratic variation (28), but a strong confirmation of this effect has not been reported. Our empirical form Eq. 2 suggests rather a direct dependence of the attempt rate with the voltage and an activation energy that is lowered proportionally to $|V|$. Such dependence has been reported in a publication combining experiments and numerical simulations qualitatively discussed in terms of the action of the field on the dipolar state of the lipids (4). If we interpret our observations within this frame and estimate the field strength by V/ℓ , the effective dipolar moment μ lowering the pore nucleation barrier is $\mu = \alpha e \ell$, where α is the coefficient in Eq. 2, e the elementary charge, and $\ell = 5 \text{ nm}$ the membrane thickness. Given the value provided by our experiments, $\alpha = 0.5$, and the (non-SI but widely used) measure of dipolar strength by a Debye unit $D = 0.02 \text{ nm}\cdot e$, we get $\mu = 125 D$, one order of magnitude larger than values reported from simulations (4). A similar analysis performed on data (21) from DPhPC membranes gives $\alpha = 0.42$, denoting a slightly smaller sensitivity of these bilayers to the formation of pores under an applied electric potential.

The voltage effect on the pore formation rate is not, in our experiments, a function of hydroperoxidation degree, contrary to the pore formation rate itself, whose dependence on X_{OOH} is shown in *SI Appendix*, Fig. S19. Thus, a fully hydroperoxidized POPC bilayer sees its activation barrier for pore formation lowered by about $5 k_B T$, with a roughly linear dependence on X_{OOH} . Simply put, full hydroperoxidation lowers the barrier for pore formation by as much as an electric field of $\sim 250 \text{ mV}$, a rule of thumb that would be interesting to correlate with the molecular transformations induced by the insertion of the $-\text{OOH}$ group in the POPC unsaturated chain (10, 29).

Long Lifetime Pores. Currents associated with large lifetime pores $\tau_p \gg \tau$ reach a stationary value which, despite the ever-present fluctuations, provides a clear distinct visual aspect to the traces. They evoke the signature of currents carried by ionic channels, which correspond in general to rather long-lived pores of a well-defined size (30). In practice, we developed a *squared gating method*—*SI Appendix*, section S7—to filter the signal $I(t)$ in order to remove noise, short lifetime pores, and complex signals. Long-lived pores are much scarcer than short-lived pores—see also Fig. 5; thus pore sizes and lifetimes collected for these pores have a larger statistical uncertainty that does not allow one, in particular, to assert the influence of voltage or oxidation degree on the frequency of pore opening. We did not find any statistical support for asserting that pores open with a fixed size—and thus conduct a fixed current—for membranes

of a given composition. There is rather a disperse distribution of currents, from where an average value can nevertheless be extracted. Significantly, the average current values follow a linear relation with applied voltage, thus enabling computation of an average pore conductance corresponding to an average pore size of $\bar{D}_p = 7.4 \pm 2.8 \text{ \AA}$, a value close to the one found for short lifetime pores. We did not find a statistically significant variation of average currents with oxidation degree. The lifetime distribution of pores lasting more than 20 ms shows, similarly to short lifetime pores, exponential decay with, however, a different time constant of 160 ms; *SI Appendix*, Fig. S18.

Conclusion

By studying conductive events across several hundreds of membranes with different hydroperoxidation degrees and by detecting and analyzing many thousands of those events, we contribute to the discussion about pore formation in lipid membranes with a new set of statistically relevant data that challenges the widely accepted V^2 dependence of the reduction of the barrier for pore nucleation and brings fresh insight to the field.

Our first finding is that the pores start opening at a voltage where the barrier model describing the intrinsic permeability of the membrane to ions stops being valid. Indeed, for low-enough voltages, the membrane maintains the nature of its permeation barrier to the ions, well described in our case by a trapezoidal model with two lengths and one height. Such a barrier corresponds to the molecular organization of the bilayer in the absence of an applied potential. When the pore formation probability becomes finite at high-enough voltages, the permeation barrier changes, implying that the lipid organization in the bilayer has changed as well. This validates numerical simulation approaches where the state of the lipids is carefully tracked, for instance, with respect to their polarization state, before opening of pores is detected.

For the large majority of events that we detected, the pore lifetime is independent of membrane oxidation. This points to explanations of pore lifetime extrinsic to the lipid membrane such as those related to the lateral relaxation of the electric stresses at the pore site, calling for further studies on the electrodissipation effects in conductive pores in lipid bilayers (22) and thus challenging whether a configuration walk in a free-energy landscape can capture the essentials of this phenomenon.

Most of the pores that we detected had small diameters, around 0.7 nm, independently of voltage or hydroperoxidation degree. The survival of such small pores over milliseconds or more suggests that they correspond to the so-called hydrophilic pores: Indeed, lipid head reorganization allowing for the head-carpeting of the inner pore canal is expected to occur tens of nanoseconds only after a water channel nucleates across the membrane (31). Geometrically, such a robust result indicates also that these pores adopt the smallest possible diameter compatible with the constraints of lipid packing in the semitoroidal inner pore surface, also supporting the anticipated deviation at small diameters of the pore line tension from its constant value.

Our results rule out a key prediction from the standard model of pore formation, namely that the barrier for pore nucleation is reduced proportionally to V^2 . Indeed, this would imply an increase in the number of pores formed during a given period of time as $\sim \exp(\text{constant} \cdot V^2)$. Under our experimental conditions, we observe instead a growth with the electric potential of the form $\sim \exp(\alpha|V|)$. Although this is compatible with explanations based on the field effect on the lipids' electric

dipoles, we find a dipolar moment one order of magnitude larger than those extracted from simulations. We anticipate much fruitful future developments along these lines to better decipher the molecular forces and membrane properties that control pore opening.

Finally, our results reinforce the picture that has been unraveling over the last decade to describe hydroperoxidized lipid membranes: Despite the strong molecular modifications that induce a larger area per lipid, smaller thickness, and a weaker stretching modulus, we find that these membranes retain their integrity, even under an applied electric potential. The work in this paper further shows that hydroperoxidized bilayers behave in a quantitatively different yet standard manner with respect to electropermeation and pore formation: They display a four-fold larger permeability with respect to the anion Cl^- and open pores with a larger frequency at weaker electric fields.

Materials and Methods

Materials. 1-palmitoyl-2-oleoyl-glycero-3-phosphocholine (POPC, 16:0:18:1) in chloroform (25 mg·mL⁻¹) was purchased from Avanti Polar Lipids. Lipids were stored at -20 °C and used without further purification; 1,9-dimethyl-methylene blue (MB), KCl, KOH, and HEPES were provided as powder from Sigma Aldrich. Cellulose membrane dialysis tubing with a molecular cutoff of 14000 Da and octane were also bought from Sigma Aldrich. All NMR analyses were performed in 99.8% deuterated methanol (MeOD) supplied by Acros Organics. To paint the free-standing lipid membranes, 10 μL pipette tips, provided from STARLAB, were used.

Lipid Hydroperoxydation. Batch solutions of POPC from fresh, i.e., sealed, POPC vials, were systematically controlled by NMR before the hydroperoxidation procedure. The two hydroperoxidized isomers of POPC-OOH shown in Fig. 1 were synthesized photochemically using MB as a photosensitizer. Briefly, 6 mL of a MeOD solution of POPC at 5 mg·mL⁻¹ (6.6 mM) containing MB at 20.8 μg·mL⁻¹ (50 μM) was placed inside a home-made device composed of red LEDs ($\lambda = 625 \text{ nm}$, 600 W·m⁻²), under a constant dioxygen flux and stirred for 10 min. Resulting conversion rates ($97 \pm 3 \text{ mol } \%$) were monitored by ¹H NMR. MB, the photosensitizer, was removed by a 4-h dialysis in water. The obtained lipid in water solution was dried, and lipids were redispersed in MeOD to perform an NMR control. Hydroperoxidized lipid solutions were kept in MeOD at -20 °C for further use.

Mixtures of POPC and POPC-OOH. MeOD solutions of POPC and of POPC-OOH were mixed as required to obtain the three targeted values of 25, 50, and 75 mol % of POPC-OOH. For each mixture, the exact POPC-OOH fraction was checked by ¹H NMR, always within $\pm 5 \text{ mol } \%$ of the target value. Solvent was then evaporated, and dried lipids were dissolved in octane at 10 mg mL⁻¹. Pure POPC and pure POPC-OOH samples were prepared in a similar manner. Lipids in octane solutions were kept at -20 °C and used within a few weeks. Here, below, results are grouped by number-weighted averages of the measured OOH content.

The Measurement Device. Experiments were performed on an Orbit Mini miniaturized bilayer workstation (Nanon Technologies, Munich, Germany), with an inserted microelectrode cavity array (MECA 4) recording chip (Ionera Technologies, Freiburg, Germany) as shown in *SI Appendix*, Fig. S1. The chip contains four wells with diameter 50 μm and depth 30 μm, each cavity corresponding to a recording channel. A chloridized silver microelectrode (Ag/AgCl) is present at the bottom of each well, and a single, macroscopic common counter electrode is found at the top of the chip.

The Orbit Mini operates in the voltage-clamp mode using the Elements 4 (e4) channel amplifier (Elements SRL, Cesena, Italy). Voltage can be imposed to only selected channel(s), but with a common value, in the range -500 mV to +500 mV. The current intensity across each well $I(t)$ is measured independently,

allowing in principle to record simultaneously the current across four different membranes. However, since the current saturation due to a membrane rupture in one of the channels induces artifact signals in the neighboring channels of the e4 amplifier, we chose to work with a single well at a time. $I(t)$ was measured with a sampling rate of 1.2 kHz and bandwidth 0.6 KHz. The Orbit Mini is piloted by elements data reader 3 (EDR 3) software, offering several measurement gains. Capacitance C_m determination uses a predefined instrument routine working with the $[-20, 20]$ nA measurement gauge. We acquired all current signals with the smallest gain, within the range $[-200, 200]$ pA.

Free Standing Bilayer Preparation. Experiments were conducted at room temperature ($\approx 20^\circ\text{C}$). The MECA 4-chip was filled with 150 μL of a fresh buffer solution composed of 100 mM KCl and 10 mM HEPES in milli-Q water, adjusted to pH 7 by addition of 1 M KOH solution, typically 10 μL for a total of 5 mL solution. Special attention was given to complete air removal from each of the four cavities. A bilayer was painted on the top of the cavity by the air bubble method described elsewhere (32). Briefly, an air bubble is formed above the chosen cavity with a 10 μL micropipette tip previously immersed in the lipid-in-octane solution. Contact with the well and further removal of the air bubble leaves attached to the rim of the aperture a thin octane film stabilized by lipids. Molecular forces lead to the thinning of the film, resulting—as schematically depicted in *SI Appendix, Fig. S1*—in a free-standing bilayer of area S in the center of the well, surrounded by a thick oil annulus attached to the rim (33). Presence, stability, and quality of the free-standing bilayer were monitored with EDR 3 under the application of ± 20 mV: A negligible current (< 0.1 pA) was seen when a sealing membrane was formed, while a saturated current (± 200 pA) was displayed otherwise. When formed, the membrane was left to equilibrate for at least 1 min while continuously checking the stability of the current. In case of an unstable current, the membrane was destroyed and reformed. Afterward, membrane capacitance C_m was measured. Capacitance variability was observed; we found that reproducible measurements were obtained for membranes with a stable capacitance ranging from roughly 6 to 13.5 pF.

Conductance Measurements. Once a membrane was formed, EDR 3 software was used to follow and record current intensity traces $I(t)$ for various imposed voltages V . A defined protocol for increasing applied voltages was applied as shown in *SI Appendix, Fig. S2*. The protocol was manually stopped at membrane rupture, corresponding to sudden irreversible current saturation. If ever a membrane resisted until reaching the sequence where $V = 500$ mV, it was not considered a valid bilayer and the experiment was discarded. The EDR 3 functionalities were first used to manually acquire a small fraction of our data before acquisition was fully automatized with a home-written macro (Pulover's Macro Creator).

We acquired currents from more than 50 membranes of each targeted lipid composition: 95 membranes for POPC containing 0% of POPC-OOH, 94 for 25%, 53 for 50%, 76 for 75%, and 55 for 100%. Statistical analysis of our data

required the development of homemade Python scripts implemented on Visual Studio. Signal treatment and pore detection techniques are further detailed in *SI Appendix*, where methods to identify and measure the different conductive modes are also discussed.

Summary of Physical Quantities.

Variable	Variable name	Units
ℓ	Membrane thickness	nm
D	Diffusion coefficient	$\text{m}^2 \cdot \text{s}^{-1}$
S	Membrane area	m^2
P_m	Permeability	$\text{m} \cdot \text{s}^{-1}$
U_m	Barrier height	Joule
K_w	Partition coefficient	Dimensionless
V	Applied potential	V
u	Reduced potential	Dimensionless
I_c	Intrinsic current	pA
i_c	Intrinsic current density	$\text{mA} \cdot \text{m}^{-2}$
I_p	Pore current	pA
D_p	Pore diameter	nm
τ	Detection response time	ms
τ_p	Pore opening time	ms
N_s	Pore opening frequency	s^{-1}
f_p	Attempt frequency	s^{-1}
C_s	Membrane capacitance	F

Data, Materials, and Software Availability. Electrophysiological data have been deposited in Zenodo (<https://doi.org/10.5281/zenodo.6944378>).

ACKNOWLEDGMENTS. E.J.L. thanks the Franco-German University and the French Ministry of High Education for a Ph.D. grant. The team is beholden to M. Basler for the development of equipment allowing fast lipid hydroperoxidation and to C. Gicquel and L. Fayolle for help with pore data analysis. Y. Moskalenko is gratefully acknowledged for support with the protocol for lipid synthesis.

Author affiliations: ^aCharles Sadron Institute, UP22, University of Strasbourg, CNRS, Strasbourg 67034, France; ^bUniversity of Lyon, CNRS, INSA Lyon, LaMCoS, UMR5259, Villeurbanne 69621, France; ^cMembrane Physiology and Technology, Institute of Physiology, University of Freiburg, Freiburg 79104, Germany; ^dlonera Technologies GmbH, Freiburg 79104, Germany; and ^eUniversity of Lyon, ENS-Lyon, Chemistry Laboratory, CNRS UMR 5182, Lyon 69342, France

Author contributions: P.M., A.P.S., J.C.B., and C.M.M. designed research; E.J.L., A.P.S., E.Z., and C.M.M. performed research; E.J.L., P.M., A.P.S., and C.M.M. analyzed data; and E.J.L., A.P.S., and C.M.M. wrote the paper.

1. D. Miklavčič, G. Serša, *Handbook of Electroporation* (Springer International Publishing, 2020), vol. 1.
2. T. Kotnik, L. Rems, M. Tarek, D. Miklavčič, Membrane electroporation and electroporeabilization: Mechanisms and models. *Ann. Rev. Biophys.* **48**, 63–91 (2019).
3. A. Hemmerle, G. Fagnetto, J. Daillant, T. Charitat, Reduction in tension and stiffening of lipid membranes in an electric field revealed by X-ray scattering. *Phys. Rev. Lett.* **116**, 228101 (2016).
4. R. A. Böckmann, B. L. De Groot, S. Kakorin, E. Neumann, H. Grubmüller, Kinetics, statistics, and energetics of lipid membrane electroporation studied by molecular dynamics simulations. *Biophys. J.* **95**, 1837–1850 (2008).
5. B. N. Ames, M. K. Shigenaga, T. M. Hagen, Oxidants, antioxidants, and the degenerative diseases of aging. *Proc. Natl. Acad. Sci. U.S.A.* **90**, 7915–7922 (1993).
6. R. Itri, C. Marques, M. Baptista, *The Giant Vesicle Book* (CRC Press, Boca Raton, FL, 2019), pp. 473–487.
7. G. Weber *et al.*, Lipid oxidation induces structural changes in biomimetic membranes. *Soft Matter* **10**, 4241–7 (2014).
8. M. Paez-Perez *et al.*, Directly imaging emergence of phase separation in peroxidized lipid membranes. *Commun. Chem.* **6**, 15 (2023).
9. Y. Guo, V. A. Baulin, F. Thalmann, Peroxidised phospholipid bilayers: Insight from coarse-grained molecular dynamics simulations. *Soft Matter* **12**, 263–271 (2016).
10. P. Siani, R. de Souza, L. Dias, R. Itri, H. Khandelia, An overview of molecular dynamics simulations of oxidized lipid systems, with a comparison of ELBA and MARTINI force fields for coarse grained lipid simulations. *Biochim. Biophys. Acta (BBA)-Biomembranes* **1858**, 2498–2511 (2016).
11. R. De Rosa, F. Spinazzi, R. Itri, Hydroperoxide and carboxyl groups preferential location in oxidized biomembranes experimentally determined by small angle x-ray scattering: Implications in membrane structure. *Biochim. Biophys. Acta (BBA)-Biomembranes* **1860**, 2299–2307 (2018).
12. A. P. Schroder, E. Zaitseva, C. M. Marques, J. C. Behrends, Voltage-dependent formation of stable, ion conductive pores in suspended lipid bilayers from oxidized lipids. *Biophys. J.* **112**, 219A (2017).
13. B. Hille, *Ionic Channels of Excitable Membranes* (Sinauer Associates, Sunderland, MA, ed. 3, 2001).
14. C. Hanneschlaeger, A. Horner, P. Pohl, Intrinsic membrane permeability to small molecules. *Chem. Rev.* **119**, 5922–5953 (2019).
15. S. W. Kowalczyk, A. Y. Grosberg, Y. Rabin, C. Dekker, Modeling the conductance and DNA blockade of solid-state nanopores. *Nanotechnology* **22**, 315101 (2011).
16. D. E. Goldman, Potential, impedance, and rectification in membranes. *J. Gen. Physiol.* **27**, 37–60 (1943).
17. A. L. Hodgkin, B. Katz, The effect of sodium ions on the electrical activity of the giant axon of the squid. *J. Physiol.* **108**, 37 (1949).
18. J. E. Hall, C. Mead, G. Szabo, A barrier model for current flow in lipid bilayer membranes. *J. Membrane Biol.* **11**, 75–97 (1973).
19. B. Fuks, F. Homble, Permeability and electrical properties of planar lipid membranes from thylakoid lipids. *Biophys. J.* **66**, 1404–1414 (1994).
20. H. Junqueira *et al.*, Molecular organization in hydroperoxidized POPC bilayers. *Biochim. Biophys. Acta (BBA)-Biomembranes* **1863**, 183659 (2021).
21. K. C. Melikov *et al.*, Voltage-induced nonconductive pre-pores and metastable single pores in unmodified planar lipid bilayer. *Biophys. J.* **80**, 1829–1836 (2001).
22. M. Winterhalter, W. Helfrich, Effect of voltage on pores in membranes. *Phys. Rev. A* **36**, 5874 (1987).
23. W. M. Haynes, D. R. Lide, T. J. Bruno, *CRC Handbook of Chemistry and Physics* (CRC Press, 2016).
24. R. W. Glaser, S. L. Leikin, L. V. Chernomordik, V. F. Pastushenko, A. I. Sokirko, Reversible electrical breakdown of lipid bilayers: Formation and evolution of pores. *Biochim. Biophys. Acta (BBA)-Biomembranes* **940**, 275–287 (1988).

25. J. T. Sengel, M. I. Wallace, Imaging the dynamics of individual electropores. *Proc. Natl. Acad. Sci. U.S.A.* **113**, 5281–5286 (2016).
26. I. Abidor *et al.*, Electric breakdown of bilayer lipid membranes: I. The main experimental facts and their qualitative discussion. *J. Electroanal. Chem. Interfacial Electrochem.* **104**, 37–52 (1979).
27. K. T. Powell, J. C. Weaver, Transient aqueous pores in bilayer membranes: A statistical theory. *Bioelectrochem. Bioenerg.* **15**, 211–227 (1986).
28. Z. Vasilkoski, A. T. Esser, T. Gowrishankar, J. C. Weaver, Membrane electroporation: The absolute rate equation and nanosecond time scale pore creation. *Phys. Rev. E* **74**, 021904 (2006).
29. P. Boonnoy, V. Jarerattanachat, M. Karttunen, J. Wong-Ekkabut, Bilayer deformation, pores, and micellation induced by oxidized lipids. *J. Phys. Chem. Lett.* **6**, 4884–4888 (2015).
30. T. Heimburg, Lipid ion channels. *Biophys. Chem.* **150**, 2–22 (2010).
31. Z. A. Levine, P. T. Vernier, Life cycle of an electropore: Field-dependent and field-independent steps in pore creation and annihilation. *J. Membrane Biol.* **236**, 27–36 (2010).
32. E. Zaitseva *et al.*, "Electrophysiology of channel-forming proteins in artificial lipid bilayers: Next-generation instrumentation for multiple recordings in parallel" in *Patch Clamp Electrophysiology* (Springer, 2021), pp. 67–92.
33. S. H. White, Analysis of the torus surrounding planar lipid bilayer membranes. *Biophys. J.* **12**, 432–445 (1972).

1

2 Supplementary Information for

3 Activation energy for pore opening in lipid membranes under an electric field

4 Eulalie J. Lafarge, Pierre Muller, André P. Schroder, Ekaterina Zaitseva, Jan C. Behrends and Carlos M. Marques

5 Carlos M. Marques.

6 E-mail: carlos.marques@ens-lyon.fr

7 This PDF file includes:

8 Supplementary text

9 Figs. S1 to S20

10 SI References

11 **Supporting Information Text**

12 **1. Measurement platform**

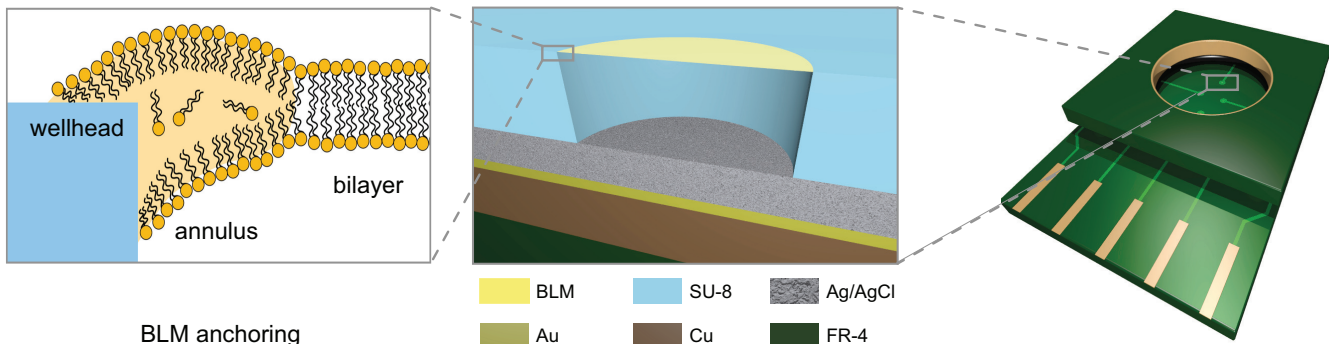


Fig. S1. The lipid bilayer on a MECA 4 recording chip. We show a vertical cut along the diameter of one of the four wells of $50 \mu\text{m}$ diameter. The painted lipid bilayer spans a large fraction of the aperture, separating a bottom from a top electrolyte solution. The presumed geometry of the anchored bilayer is also illustrated. Thickness of the gold bottom electrode increased for clarity.

13 In MECA 4 chips used in this work the lipid bilayer of surface S occupies the central part of a thin film painted from an
 14 oil-lipid mixture. As shown in Fig. S1, the film is anchored to the edge of a well of $50 \mu\text{m}$ diameter corresponding to a well
 15 aperture surface of $1963 \mu\text{m}^2$. The anchoring rim (annulus) is better described as a thin oil film stabilized by lipids, while the
 16 bilayer in the center is believed to contain a very small fraction of solvent. Since the rim region, that extends a few micrometers
 17 from the edge of the well, is too thick to contribute to the electric response of the membrane, one can in principle measure
 18 the bilayer surface from the measurement of the bilayer capacitance, if all the bilayers have the same specific capacitance
 19 c_m . This was assumed throughout the paper, with the value asserted in the membrane capacitance section of the main paper
 20 $c_m = 6.9 \text{ mF} \cdot \text{m}^{-2}$, see also Fig. S5 below for measured values.

21 In general, presence of organic solvent in the lipid bilayer is known to lower its specific capacitance (1), so variations of the
 22 observed capacitance values in our apparatus could in principle be due to a variable amount of octane trapped in the bilayer.
 23 Thermodynamic arguments suggest that if some finite fraction of oil is present in the bilayer, it should be a constant throughout
 24 all layers of same lipid composition. Indeed, the bilayer part of the film, which is in a fluid state at room temperature, can be
 25 seen as a well-defined thermodynamic state governed by the local molecular forces, connected to, and in equilibrium with, the
 26 large oil reservoir hosted by the rim: the oil chemical potential in the bilayer is thus fixed by the reservoir, and can be assumed
 27 to be a constant.

28 In our experiments, for POPC, the ratio between the larger and the smaller measured values of the capacitance C_m is
 29 $13.5/6=2.25$. Assuming that the largest value corresponds to a bilayer of $50 \mu\text{m}$ diameter with a vanishingly small rim, the
 30 smallest measured bilayer with an assumed identical specific capacitance would have a diameter of $33 \mu\text{m}$. According to the
 31 same assumptions, the surface corresponding to the average POPC capacitances shown in Fig. S5 has a diameter of $42 \mu\text{m}$, or
 32 equivalently a rim with lateral dimension $4 \mu\text{m}$. Despite having a well-defined average, capacitances span thus a rather large
 33 range of values, about 50 % above and below average, with equivalent dispersions for the corresponding surfaces and about
 34 25 % for the diameter. We believe that the main reason for observed capacitance variations or the bilayer /annulus ratio in
 35 our experiments is the variable amount of lipid solution which is present near the cavity during the manual bilayer formation.
 36 Other reasons can be hypothesized as being related to the draining process of the solvent during the painting process, but also
 37 as being associated with the quality of surface of the well in the aperture region. Fig. S20 shows an optical microscopy image
 38 of one of the wells used for our experiments. Small geometrical irregularities can be seen at the level of the well opening that
 39 certainly play a role in the anchoring of the film to the wall. Thus, in the discussion of our results in the main text, variability
 40 of traces should come as no surprise, given the heterogeneity of the formed membrane that adds an external source of noise to
 41 the intrinsic stochasticity of the transport processes that are analyzed here.

42 With this platform we measure current traces such as those displayed in Fig. 2 and further discussed and exemplified here in
 43 the supplemental sections. The most robust observation for all the traces is that conduction is always present in a continuous
 44 manner, as an average small ($\sim \text{pA}$) current value “decorated” by additional current fluctuations of limited but measurable
 45 amplitude $\sim 2 \text{ pA}$. This current corresponds to the non-localized transport of individual charges across the membrane, a
 46 measure of the membrane intrinsic permeability with respect to the electrolyte, here KCl. Additionally to this average current
 47 a number of other conductive events can be detected, of variable amplitude and duration. Irrespective of their precise nature, a
 48 general trend is observed that corresponds, for each oxidation degree to an increase of charge transfer as a function of voltage
 49 and, for each voltage, to an increase of charge transport as a function of the degree of oxidation. An asymmetry in the traces
 50 can also be observed that favors charge transport when the electric potential is negative, that is when it drives K^+ ions from the
 51 large volume ($\sim 150 \mu\text{L}$) above the membrane into the 60 pL well below the membrane, and correspondingly drives Cl^- ions in
 52 the opposite direction. Such asymmetry is possibly induced by one or a combination of the several intrinsic asymmetries of the
 53 Meca 4 chip: different volumes above or below the membrane, membrane anchoring at the edges of the well, electrochemistry

54 events at the electrode in this well. The asymmetry has a limited impact on our observations and it does not preclude a precise
 55 quantitative analysis of the results.

56 2. Ramping voltage protocol

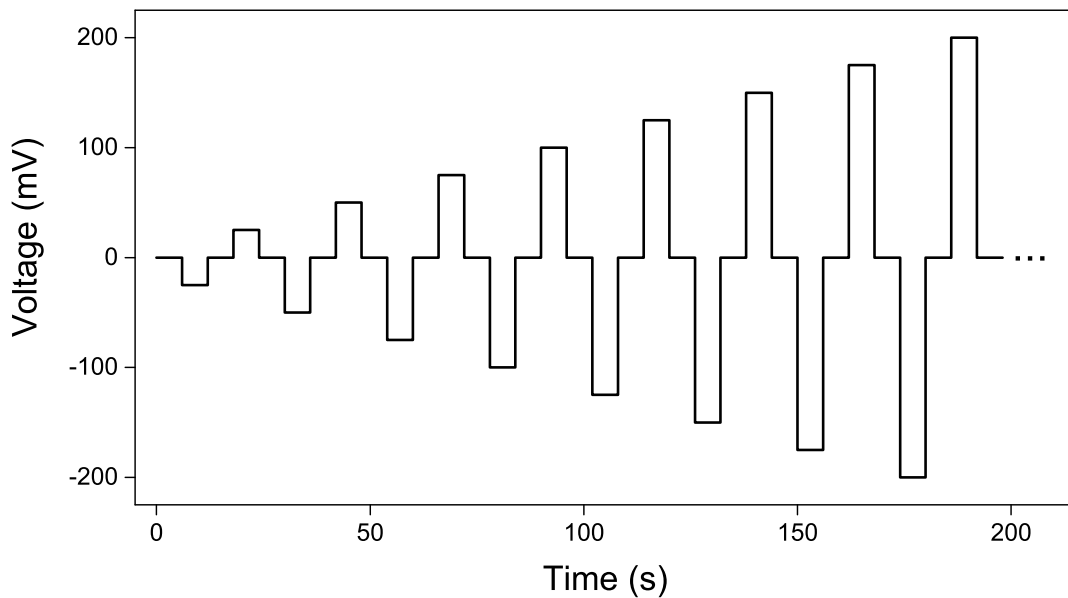


Fig. S2. Voltage protocol $V(t)$ used for current intensity recordings. Voltages were increased from 0 mV to 500 mV by steps of 25 mV. At each step negative and positive voltages were applied during 6 seconds, separated by a relaxation of 6 seconds at 0 mV between each applied voltage. One thus have 24 seconds sequences for each step of the applied voltage and a maximum of 20 possible sequences until the maximum possible voltage of 500 mV is reached, for a total maximum possible experiment duration of 480 seconds.

57 3. The measurement platform as an electric circuit

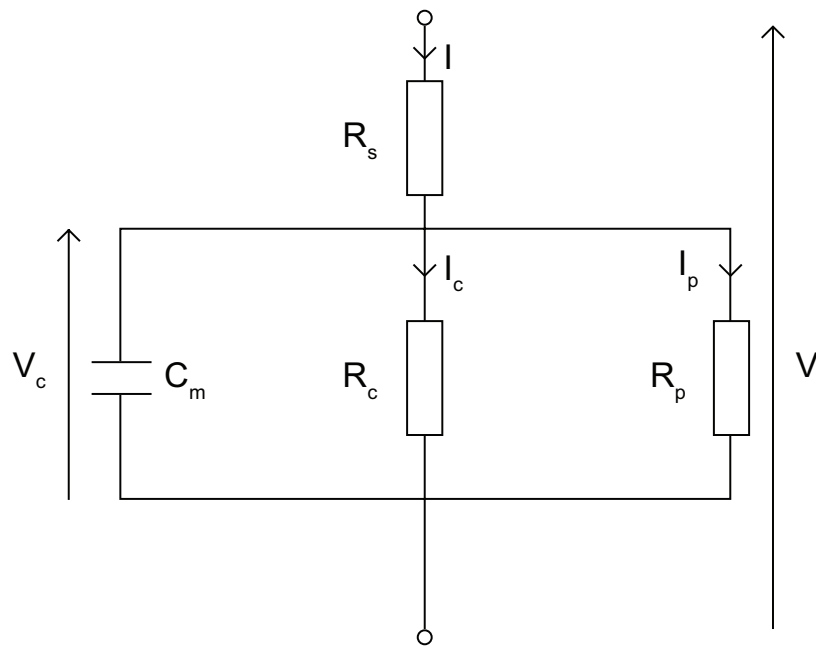


Fig. S3. Equivalent electric circuit for a free standing bilayer. R_s is the instrument resistance, that also includes the electrolyte. C_m is the membrane capacitance, R_c is the intrinsic membrane resistance in absence of pores through which flows a current I_c . When a pore opens, an added current I_p flows through the pore resistance R_p . The instrument works in a voltage clamp mode where the potential difference V is kept constant.

58 **A. Capacitive relaxation times are much smaller than sampling times.** The minimal representation of the equivalent electric
 59 circuit of our measurement platform (2–4) is depicted in Fig. S3. The values of $V(t)$ follow typically the time evolution shown
 60 in Fig. S2. The pore resistance is also a function of time $R_p(t)$. In the simplest pore models where the pore stays open at
 61 a constant diameter for a duration τ_p , from an initial time t_i , one has $R_p(t) = R_p$ for $t_i < t < t_i + \tau_p$ and with $R_p(t) = \infty$
 62 otherwise.

63 The potential difference $V_c(t)$ at the capacitor follows the differential equation

$$64 C_m \frac{dV_c(t)}{dt} = -V_c(t) \left(\frac{1}{R_s} + \frac{1}{R_c} + \frac{1}{R_p(t)} \right) + \frac{V(t)}{R_s} \quad [1]$$

65 Straightforward integration of Eq. 1 provides a solution for $V_c(t)$, and for the current measured by the instrument
 66 $I(t) = (V(t) - V_c(t))/R_s$. Of particular interest for us is the current flowing under a potential V applied at time 0. After the
 67 pore opens: $t_i < t < t_i + \tau_p$. Assuming that the pore opening time t_i is much larger than the time needed for the membrane to
 68 charge, i.e. $t_i \gg \tau_{RC} = C_m(R_s^{-1} + R_c^{-1})^{-1} \simeq C_m R_s$ one has

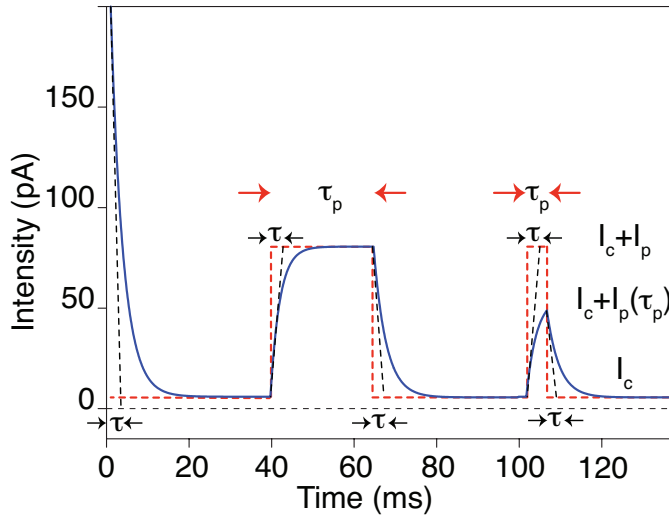
$$69 I(t) = \frac{V}{R_s} \left[1 - \frac{R_c}{R_s + R_c} \exp \left(-\frac{t - t_i}{\tau_d} \right) - \frac{R_m}{R_s + R_m} \left(1 - \exp \left(-\frac{t - t_i}{\tau_d} \right) \right) \right] \quad [2]$$

70 with $R_m^{-1} = R_c^{-1} + R_p^{-1}$ the membrane resistance when a pore is open and $\tau_d^{-1} = C_m^{-1}(R_s^{-1} + R_m^{-1})$ the circuit time constant
 71 when a pore is open. After the pore closes, for $t > t_i + \tau_p$, the intensity decays towards the stationary value it had before the
 72 pore opened, following

$$73 I(t) = \frac{V}{R_s} \left[1 - \frac{R_m}{R_s + R_m} \exp \left(-\frac{t - (t_i + \tau_p)}{\tau_{RC}} \right) - \frac{R_c}{R_s + R_c} \left(1 - \left(1 - \exp \left(-\frac{\tau_p}{\tau_d} \right) \right) \exp \left(-\frac{t - (t_i + \tau_p)}{\tau_{RC}} \right) \right) \right] \quad [3]$$

74 If the pore opens for a long enough time ($\tau_p \gg \tau_d$), the current rises thus from its stationary value $V/(R_s + R_c) \simeq V/R_c$ to
 75 a higher stationary value $V/(R_s + R_m) \simeq V/R_m \simeq V/R_p$ while the potential at the capacitor decreases from the stationary
 76 value $VR_c/(R_s + R_c) \simeq V(1 - R_s/R_c)$ to a slightly smaller stationary value $VR_m/(R_m + R_s) \simeq V(1 - R_s/R_m)$. If the pore is
 77 short lived ($\tau_p \ll \tau_d$) one cannot directly evaluate the pore resistance R_p , or correspondingly I_p , the current that would have
 78 been reached in the stationary state. I_p can still however be evaluated by measuring the largest value of $I(t)$ reached during
 79 pore opening. Assuming that the maximum is reached for $t - t_i = \tau_p$, one can numerically solve Eq. 2 to extract I_p . In our
 80 case τ_{RC} is of order of microseconds and the observations are made at a sampling rate of 1.2 kHz, so all capacitive relaxations
 81 are much faster than the observation time step of 0.8 ms.

B. Signal relaxation is dominated by filtering.



82 **Fig. S4.** Completely and partially developed pore signals. Under our sampling and filtering conditions (sample rate of 1.2 kHz and bandwidth of 610 Hz), current variations relax
 83 with a roughly exponential decay function and a characteristic decay time $\tau \simeq 2.7$ ms. The current from pores with large enough lifetimes ($\tau_p \gg \tau$) reaches a stationary state.
 84 The size of the pore can be computed from the stationary value of the current I_p . For shorter pore lifetimes ($\tau_p \ll \tau$) the current cannot reach its stationary value I_p , but I_p
 85 can still be evaluated by measuring the intensity at time τ_p and assuming that it follows a rising exponential with rate τ .

86

87 4. Capacitance values

88 We measured capacitances C_m for all membranes studied here, see Fig. S5. In the present geometry, C_m mainly depends on
 89 the lateral extension of the oil annulus attaching the bilayer to the rim of the aperture. Assuming a negligible annulus, i.e.

86 $S = S_{\max} = \pi \times 25^2 \simeq 1963 \mu\text{m}^2$) for the maximum measured value $C_m = 13.5 \text{ pF}$ one gets $c_m = C_m/S = 6.9 \text{ mF}\cdot\text{m}^{-2}$ for the
 87 specific capacitance of POPC, within the range of reported values (1, 5–8). As the figure shows, hydroperoxidation has no
 88 statistically significant impact on bilayer capacitance. In the main paper we interpret capacitance variations as resulting only
 89 from variations in the surface S of the free standing bilayer and use the measurement of C_m as a surface measurement.

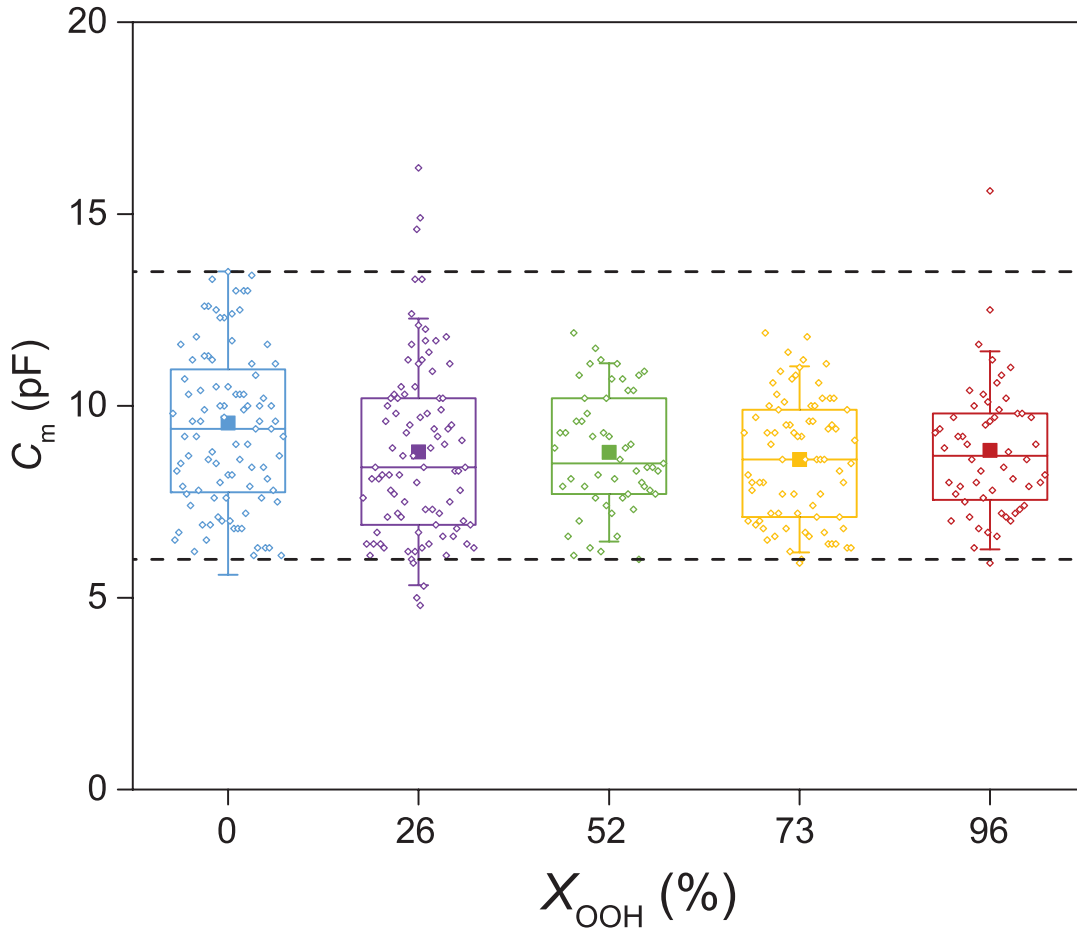


Fig. S5. Capacitance values of the investigated bilayers. The box-plot represents the distribution of membrane capacitance based on first quartile, median, mean (filled square symbol), third quartile, with whiskers showing standard deviation.

90 Studies of the specific capacitance of POPC are scarce. Indirect measurements from shape transitions induced by an
 91 oscillatory electric field in solvent-free GUVs (7) give $c_m = 5.0 \text{ mF}\cdot\text{m}^{-2}$, but patch-clamp results from GUVs of DOPC (a lipid
 92 with two more carbons and one unsaturated bond more than POPC) and of SOPC (two more carbons in the saturated tail
 93 than POPC) give larger values at $c_m = 8.7 \text{ mF}\cdot\text{m}^{-2}$ and $c_m = 7.8 \text{ mF}\cdot\text{m}^{-2}$ respectively (5). Measurements by the droplet
 94 interface bilayer (8), where, similarly to our system, the bilayer is exposed also to an oil reservoir give $c_m = 6.8 \text{ mF}\cdot\text{m}^{-2}$ for
 95 POPE, a lipid with the same tail architecture as POPC but with a different headgroup. This certainly reinforces our choice of
 96 $c_m = 6.9 \text{ mF}\cdot\text{m}^{-2}$ based on our maximum measured value of C_m and on the maximum possible surface S_{\max} and consistent
 97 with the one slab model where $c_m = \epsilon_0 \epsilon_m/b$, with ϵ_0 the vacuum permittivity, ϵ_m the membrane relative permittivity and b
 98 the slab thickness. With the typical value $\epsilon_m = 2.1$ for oils with chain lengths comparable to POPC and the hydrophobic core
 99 thickness $b = 2.7 \text{ nm}$ (9) one gets $c_m = 6.9 \text{ mF}\cdot\text{m}^{-2}$.

100 As we stressed before, we were able to paint a total of hundreds of lipid bilayers from mixtures of POPC and POPC-OOH at
 101 any arbitrary composition, contrary to results reported in (10). This might be due to the quality and size of our wells, which are
 102 smaller than some of other studies previously reported, or simply due to the systematic use of freshly hydroperoxidized samples
 103 in our experiments. Unexpectedly, as S5 shows, we found that the capacitance does not depend on the hydroperoxidation degree
 104 of the membrane. Given the smaller thicknesses of the oxidized membranes, and the expected larger dielectric permittivity of
 105 their hydrophobic core, one would anticipate, within the one slab model, an increase of capacitance with X_{OOH} , the fraction
 106 of OOH groups. The changes in the structure of the membrane are however complex: an important fraction of the tails
 107 bearing -OOH groups adopt a snorkeling configuration, thus changing not only the hydrophobic core in a non-trivial manner,
 108 but changing also the structure of the head region where the area per head is increased and OOH groups are added to the
 109 interface (11–14). That these effects balance to keep a constant specific capacitance poses an interesting question, into which
 110 all-atom simulations might provide some insight.

111 **5. Typical traces**

112 Examples of traces from our system are shown on Fig. S6 for three different fractions of oxidized lipids (0 %, 50 % and 100 %)
 113 and for six different applied voltages (± 50 mV, ± 100 mV and ± 150 mV). Traces for pure POPC and 50 % mixtures compare
 114 well with results from (10) who did not report results for 100 % POPC-OOH. Traces displayed represent many of the features
 115 described next. Given the stochastic nature of phenomena discussed here, visual aspect of the traces vary strongly from
 116 experiment to experiment even under the same conditions.

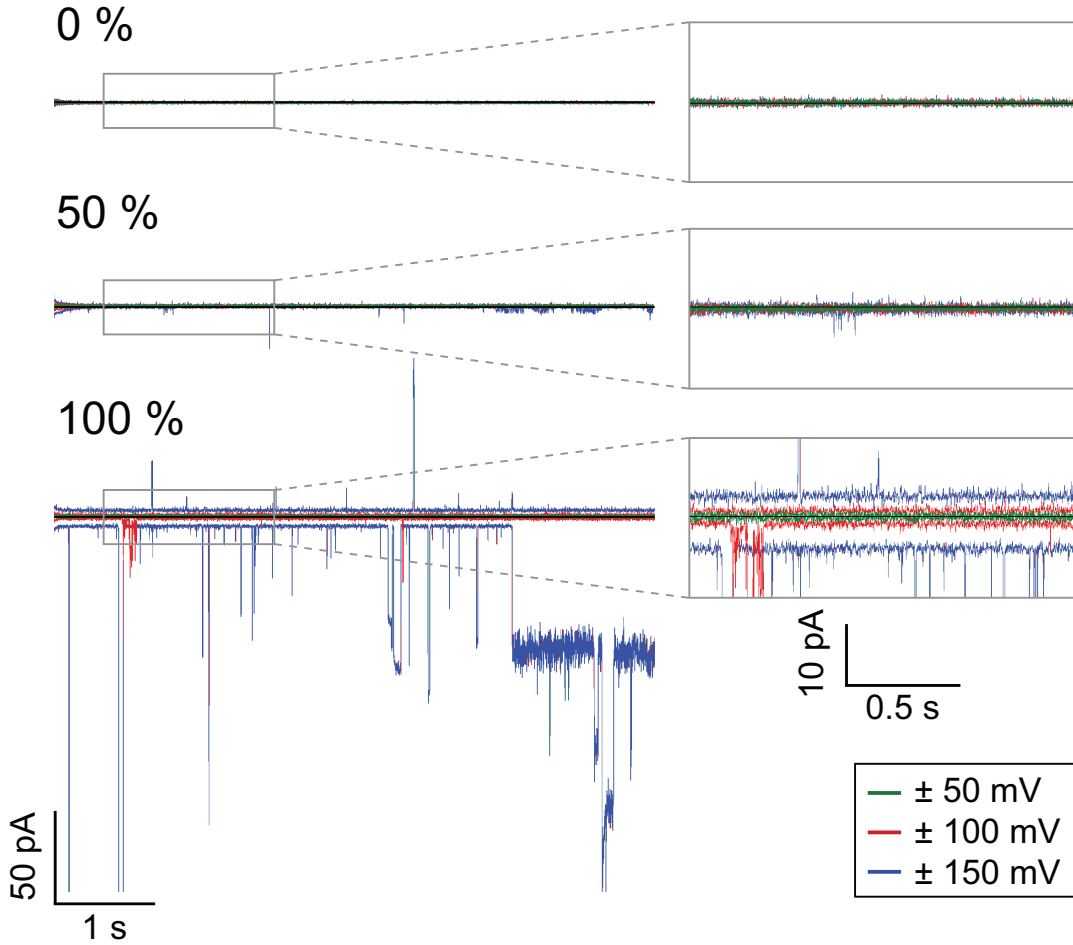


Fig. S6. Examples of current intensity traces $I(t)$. Data recorded under voltage-clamp conditions for POPC membranes containing 0 %, 50 % or 100 % of POPC-OOH with applied voltages of ± 50 mV, ± 100 mV and ± 150 mV. Expanded traces are shown in the right panels.

117 **6. Identifiable pores and other events**

118 In the standard theory of pore formation two types of pores are distinguished. The pores that form first are designated as
 119 *hydrophobic pores*, they correspond to a simple "hole" in the membrane, with the water tunnel connecting both sides of
 120 the membrane exposed to the phospholipid tails – thus the "hydrophobic" designation. These pores, are considered to have
 121 diameters smaller than 1 nm and to be only metastable since they either close rapidly (in the nanosecond range, thus not
 122 observable by our experiments) or evolve into *hydrophilic pores*. Phospholipids involved in the formation of larger pores have
 123 reorganized in such a way that now all the pore surface is carpeted by phospholipids heads as shown in sections (iii) and (iv) of
 124 Fig. 3. Thus, they have properties closer, but still somewhat different – for instance they are in a curved geometry – from
 125 lipids away from the pore. Since head-lipid reorganization is a longer process, these pores are considered to be longer-lived
 126 than their hydrophobic counterparts. Computer simulations on pore formation confirmed this early intuition of the standard
 127 model of pore formation, while enriching and nuancing such simple description with further molecular details (15).

128 In order to provide for a finer description of the pores opened by the membranes we classified pores in three different
 129 categories. When the opening of a new pore can be identified, like those in sections (iii), (iv) and (v) of Fig. , even if other
 130 pores are already opened, we name the pore "short lifetime pore" when it closes in a time τ_p less than 10 ms – roughly three
 131 times the equivalent electrical circuit time τ_{RC} – and we name it "long lifetime pore" if $\tau_p > 20$ ms (twice the upper cutoff of
 132 the shorter events duration for proper separation of the signals). All other types of conduction events are grouped as a third

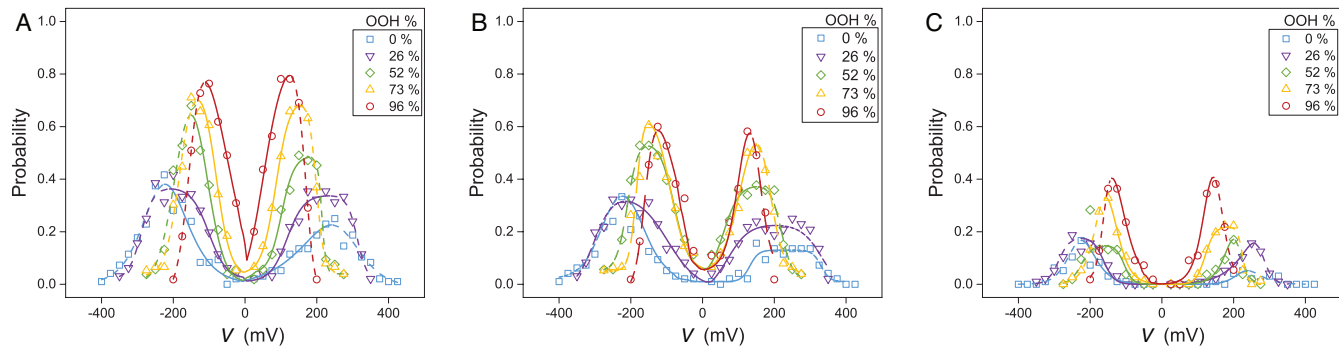


Fig. S7. Membrane probability to open (A) short, (B) long lifetime pore or (C) exhibiting complex behaviour at different voltages and lipid hydroperoxidation degree. Symbols are the experimental probabilities; solid lines are simple visual guide line for relevant probabilities and dashed lines the visual guide for biased data due to membrane rupture.

133 class, where a correspondence between the type of trace and the state of the membrane cannot be established. The probability
134 for a membrane to open a pore of each of these three categories has been determined for every applied voltage and membrane
135 peroxidation degree and displayed in Fig. S7.

136 As the figure shows, the opening probability increases with voltage for all classes of pores. Due to membrane rupture,
137 the curves reach a maximum before declining to zero. The shape of the probability curves is also indicative of significant
138 heterogeneity in membrane behavior, since often membranes surviving to higher voltages also open less pores.

139 By number, short lifetime pores are predominant, they are nearly seen in every membrane. On the contrary, long lifetime
140 pores appeared unevenly distributed among the traces of different bilayers of a given membrane composition. For some bilayers,
141 long pores seldom open, while others systematically display long pores over the full sequence of applied voltages.

142 Clearly, short lifetime and long lifetime pores open over the same voltage range (compare Figs. S7 A and S7 B). Membranes
143 of each composition were able to open pores of every category, with a net increase of the pore opening probability with
144 hydroperoxidation degree. More complex signals are triggered by slightly higher voltages but do form for all membrane
145 compositions.

146 7. Pore detection and signal filtering

147 Pore detection algorithms can be found in literature, that were mostly developed for conductivity recordings of ion channels, *i.e.*
148 characterized by well-defined intensity plateaus. Those algorithms cannot be transposed for the analysis of our current signals,
149 that exhibit a large variety of peaks, with complex duration and intensity patterns (16). Beside, various models exist, to filter
150 current intensity signals, but again, rare are the ones being relevant for analyzing our complex traces (17). We developed two
151 algorithms, devoted i) to the analysis of single, isolated pore events and ii) to the analysis of complex current traces displaying
152 two or more coincidental pores. It is worth noting that none of those algorithms can be applied without human action. In
153 order words, each algorithm was applied on wisely selected sub-recordings of constant applied voltage, that were identified as
154 corresponding to one of the latter two situations. For a matter of convenience, both algorithms work with positive signals, *i.e.*
155 the intensity signals corresponding to negative voltages were inverted before analysis.

156 **Isolated pore detection.** The algorithm requires as an input parameter the threshold intensity cutting off intrinsic fluctuations.
157 In practice, we measure the spontaneous signal fluctuations around the average I_c and chose the threshold value well above
158 fluctuations – see dashed red line in Fig. S8. The signal noise can vary from one experiment to the other, and one needs to
159 adjust accordingly the detection threshold.

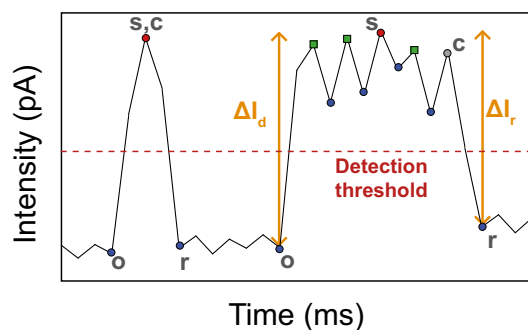


Fig. S8. Scheme of the automatic detection of opening time, closing time and intensity for two isolated pores.

160 Starting from a signal region devoid of pores, the algorithm scans the trace up to the first local maximum above the detection

threshold, as shown in Fig. S8 for two successive pores. Scanning continues, with the identification and storage of every local maximum until the closing of the pore is detected, characterized by the return of the intensity back to a value below the detection threshold (points **r** in Fig. S8). We tag the opening time of a detected pore as the last point with an intensity value below threshold, after we detect the first maximum (points **o** in Fig. S8); correspondingly, we tag the closing time as the last local maximum before point **r** (points **c** in Fig. S8). Between points **o** and **r**, the maximum value of the signal is taken as the reference for the pore intensity (points **s** in Fig. S8). Then ΔI_o is calculated as $I(\mathbf{r}) - I(\mathbf{o})$ while ΔI_r is calculated as $I(\mathbf{s}) - I(\mathbf{r})$. If those two quantities differ by more than 50%, the pore is discarded, otherwise the intensity of the pore I_p is calculated as the max[$\Delta I_o, \Delta I_r$]. The pore lifetime τ_p is calculated as the difference between closing $t(\mathbf{c})$ and opening $t(\mathbf{o})$ times. The shortest lifetimes are obtained when points **c** and **s** coincide. Please note that noise in the baseline signal can induce an error of one time interval (here 0.8 ms) in the definitions of both **o** and **s**. Note also that the algorithm overestimates pore current by a value comparable to the amplitude of open pore fluctuations, since for simplicity the maximum of the current (point **s**) is chosen for its calculation (Fig. S9).

The isolated pore algorithm was used to build the pore lifetime distribution shown in Fig. 6. An analysis of data restricted to pores with a lifetime smaller than 10 ms provided the short lifetime pore analysis discussed in the main text.

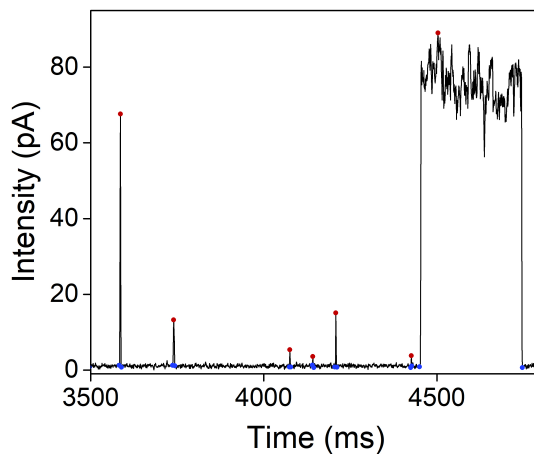


Fig. S9. Example of detection of time isolated pores.

Multiple pore detection. A second algorithm was developed to analyze signals carrying the signature of two or more pores opened simultaneously over some time period. The algorithm delivers a filtered signal with well defined intensity plateaus of a duration >20 ms. Thus, intensity jump events shorter than 20 ms are ignored, while regions of equal intensity, up to noise contributions, are replaced by the intensity average over those regions. This filtering method requires the value of the noise as an input parameter. To take into account the fact that the signal exhibits an increasing noise with intensity, the algorithm calculates a local noise $N_{\text{loc}}(I)$ for each intensity I during its exploration of the signal. A linear law of the form $N_{\text{loc}}(I) = N_0(1 + I \cdot G_{\text{noise}})$ was found to fit well the data. The values $N_0=5$ pA and $G_{\text{noise}}=0.02$ were often used, but were adapted if necessary for the signal under study. Fig. S10 shows an example of signal filtering according to this method.

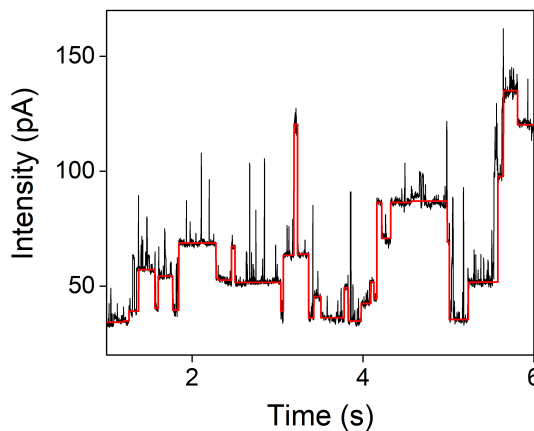


Fig. S10. Example of signal filtering for long lifetime pore detection.

183 **8. Membrane rupture**

184

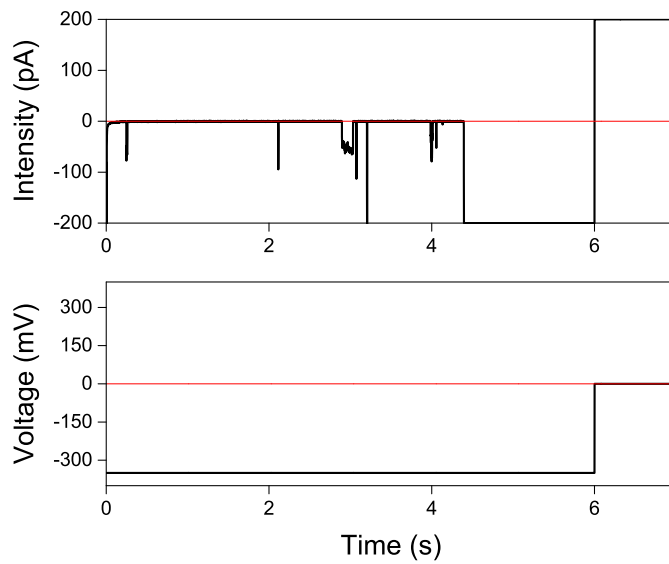


Fig. S11. The typical I-V signatures of a membrane rupture event, here for POPC.

185 Evidence of membrane rupture is brought by an irreversibly saturated signal (positive or negative), at the maximum gauge
186 value, here ± 200 pA. Irreversible saturation is detected by bringing the imposed voltage close to zero and verifying whether
187 saturation persists. An example is given in Fig. S11, where the current intensity saturates after ≈ 4.5 s of application of a
188 -325 mV voltage, something that could either be interpreted as the creation of a large ($D_p > 1.8$ nm) pore, or by the membrane
189 rupture. Rupture is confirmed by the persistence of the saturated current when the applied voltage is brought to zero.

190 **9. Membrane survival probability**

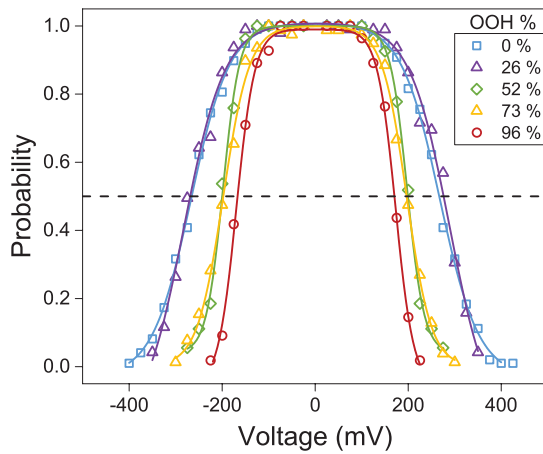


Fig. S12. Membrane survival probability. Symbols represent the calculated probability, solid lines are a visual guide only.

191

192 Optimal data acquisition in these studies requires not only painting stable membranes, but also being able to increase the
193 applied potential and collect data without membrane bursting. The quantitative evaluation of membrane survival probability
194 under an electric field shown in Fig. S12 provides an useful guide for experiments planning. Survival probability measured for
195 instance as the value of the applied potential at 1/2 probability decreases irregularly with X_{OOH} . Given the more regular
196 behavior of, for instance, the probability of pore opening seen in Fig. 5 it is likely that membrane survival depends not only on
197 the intrinsic mechanisms for nucleation and growth of pores but also on other factors such as the heterogeneity of membrane
198 anchoring discussed above. Direct trace analysis provides also some insight into the disruption mechanisms of the membrane. A
199 striking feature of the bursting events is the abrupt character of current increase, with signal rising from a few pA to saturation

at 200 pA in a couple of milliseconds. If associated with pore opening and expansion, this implies expansion velocities \dot{D}_p of the pore diameter larger than one $\mu\text{m}\cdot\text{s}^{-1}$ in the range 0-3 nm (0-200 pA), compatible with measurements at the larger optical scales where pore opening has been measured at velocities $\sim \text{mm}\cdot\text{s}^{-1}$ (18). Another common feature with pore opening at larger scales is pore resealing. For most of the X_{OOH} values studied here, a finite fraction (20 % - 50 %) of saturation events are reversible, showing that under the applied potential pores larger than 3 nm form that can reseal after reduction or inversion of the potential. As a general trend for all X_{OOH} values, we found that the maximum voltage that a membrane can withstand decreases as membrane capacitance increases: larger membranes are disrupted at smaller applied voltages (data not shown). This corroborates our hypothesis that our 50 μm well allows painting and measuring membranes that would be harder to obtain in devices with cavities of larger diameters. However, as Fig. S5 shows, there is no correlation between the size at which membranes form and their oxidation degree. The systematic decrease of rupture voltage with X_{OOH} applies therefore across the whole capacitance distribution.

10. Pore emergence is related to a strong modification of the membrane structure

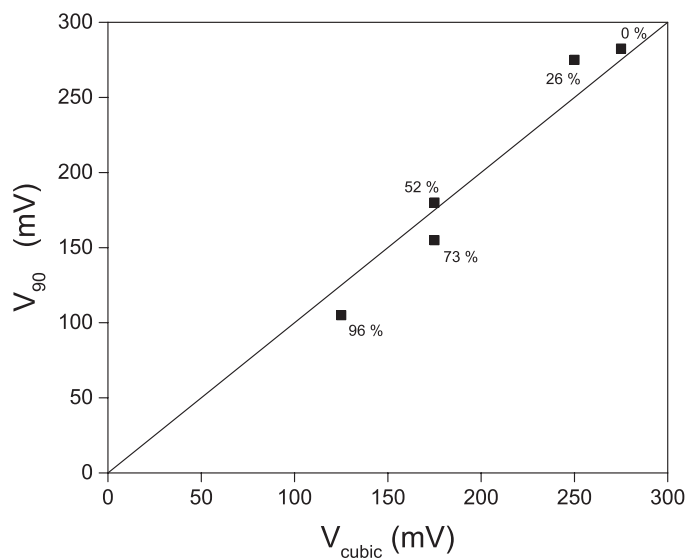


Fig. S13. Pore opens when the voltage is high enough to distort the intrinsic membrane barrier to ions. X_{OOH} values are given for each corresponding data point.

As reported in the main text, the supralinear behavior of $I_c(V)$ cannot be accurately described by (Eq.1) above (resp. below) a given positive (resp. negative) voltage, that depends on X_{OOH} . We call V_{cubic} this limit value, that can be determined in Fig. 4 as the limit between the continuous and dashed lines. We further define V_{90} as the voltage at which a membrane of a given X_{OOH} has 90% chance to open at least one single pore during the 6 sec duration of application of this voltage. Values of V_{90} can be determined in Fig. 5 from the intercept between the horizontal dashed line and the corresponding probability bell-shaped curve. Fig. S13 shows the correlation between V_{cubic} and V_{90} .

11. Average pore lifetime is independent of voltage and hydroperoxidation degree

As defined in the main text, section 'Identifiable pores and other events', we detect and measure the individual lifetimes $\tau_p(V)$ for all identifiable pores created at voltage V for each X_{OOH} . We then average all $\tau_p(V)$ for a given V and X_{OOH} . The average values $\langle \tau_p(V) \rangle$ are shown in figure below Fig. S14, and do not display any significant dependence on either voltage or peroxydation degree.

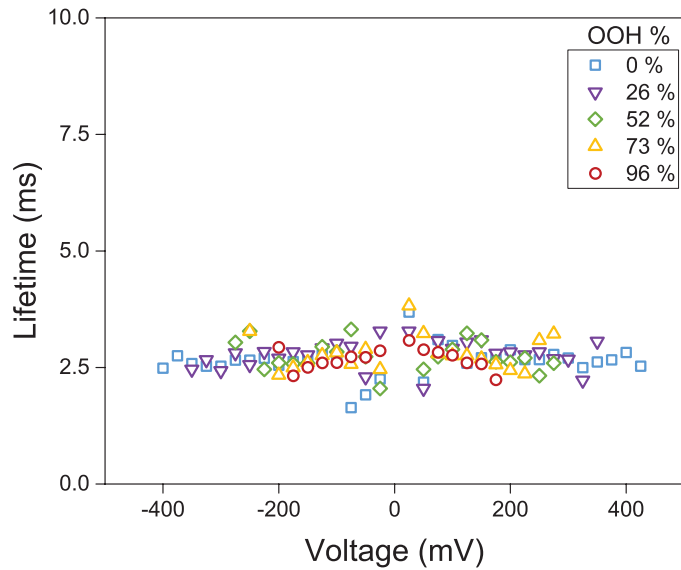


Fig. S14. Average pore lifetime $\langle \tau_p(V) \rangle$ as a function of voltage for the five hydroperoxidation degrees.

223 12. Pore contribution to membrane conductivity

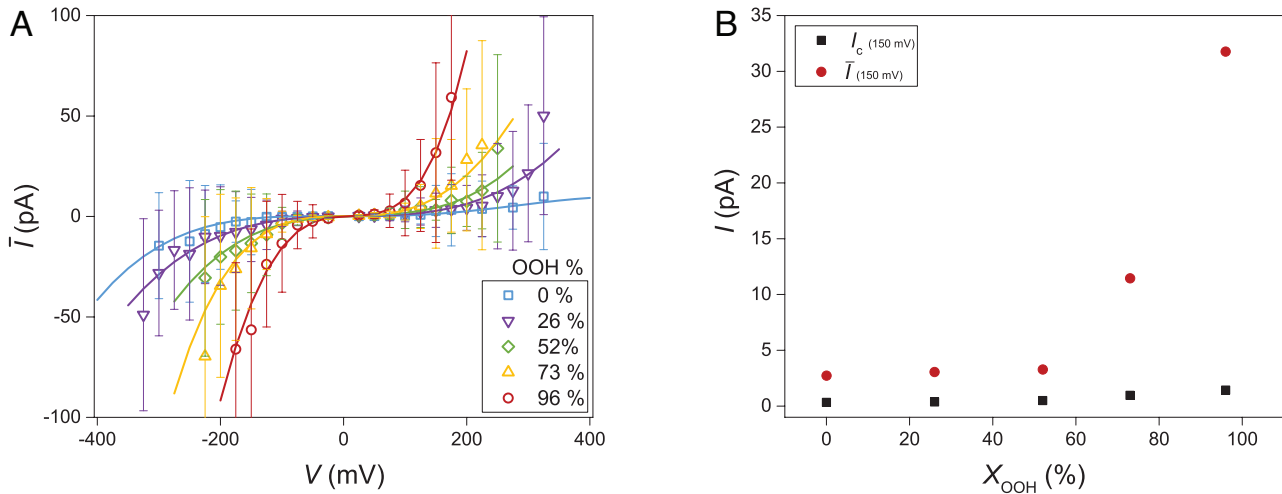


Fig. S15. (A) mean current intensity as a function of the applied voltage for the different lipid membrane compositions. Error bars represent standard deviation. (B) comparison between I_c and \bar{I} taken at 150 mV, in function of peroxidation.

224

Average overall conductivity \bar{I} of the membrane is obtained by averaging the current I crossing the membrane over the six seconds during which voltage is applied, irrespective of the events that generated the signal. Fig. S15 A presents $\bar{I}(V)$ for the five POPC/POPC-OOH compositions. $\bar{I}(V)$ curves are supralinear, similarly to $I_c(V)$ in Fig. 4. However, $\bar{I} \gg I_c$ showing the dominant contribution of membrane pores to the total amount of charge crossing the membrane for large enough applied voltages. As an example, Fig. S15 B compares I_c and \bar{I} variations with X_{OOH} at 150 mV. As the figure shows, hydroperoxidation contributes not only to larger values of the intrinsic permeability but also to a very significant increase in pore opening, as also reported previously (10).

232 **13. Diameter distribution of short lived pores**

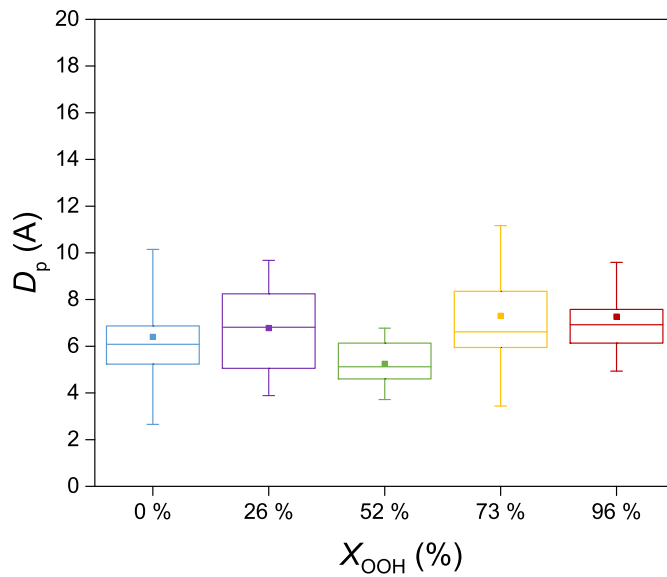


Fig. S16. Average pore diameter of short lifetime pores for different hydroperoxidation degree. Values are shown for all applied voltages since no dependence of pore resistance R_p was found on V. The filled square represents the average, the middle line the median, the edges of the box the first and third quartile and the whiskers the standard deviation.

233 In order to obtain a rough distribution for the pore current values we set pore lifetime τ_p at its average value 2 ms, the
 234 capacitance C_m at the average value 9 pF and the circuit constant at 3 ms (from data not shown). I_c values (remember
 235 $I = I_c + I_p$) where extracted from their average values measured before and are dependent on X_{OOH} . Results are shown in
 236 Fig. S16 as diameter distributions obtained from the I_p distributions with $R_p = V/I_p$ and $D_p = (4b/\pi R_p \sigma)^{1/2}$ with $b = 5$ nm
 237 the thickness of the pore and σ the solution conductivity, $\sigma = 1.29$ S.m⁻¹ for a 100 mM KCl solution (19, 20).

238 **14. Diameter distribution of long lived pores**

239 From long lifetime pores, the average pore diameter can be determined directly from the traces for each voltage and
 240 hydroperoxidation degree. The pore resistance and thus the diameter was found to do not depend on the voltage neither on
 241 the hydroperoxydation degree as seen in Fig. S17.

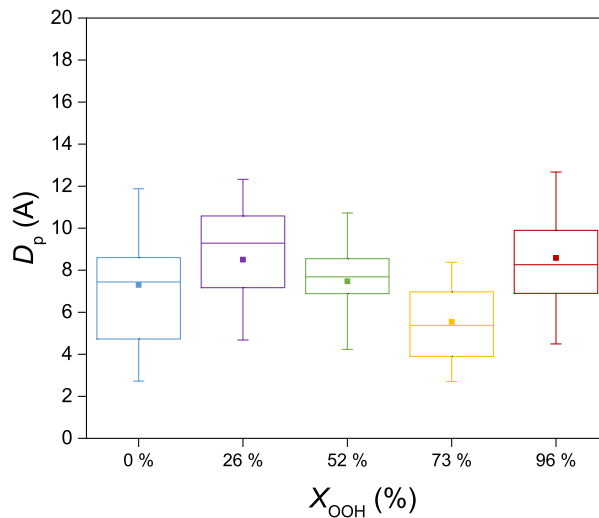


Fig. S17. Average pore diameter of long lifetime pores over the different voltages for different hydroperoxidation degree. The filled square represent the average, the middle line, the median, the edges of the box the first and third quartile and the whiskers the standard deviation.

242 **15. Lifetime distribution of long lived pores**

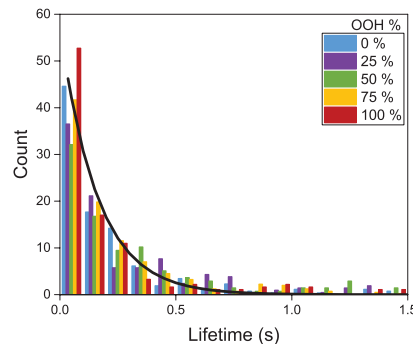


Fig. S18. Pore lifetime distribution for long lifetime pores detected with the squared signal idealization technique

243

244 **16. Dependence of pore opening frequency on hydroperoxidation degree**

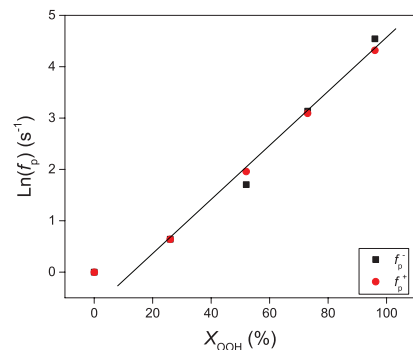


Fig. S19. Pore opening frequency for positive f_p^+ and negative f_p^- voltages for the different hydroperoxydation degree of membranes.

245

246 **17. Optical micrograph of measurement well**

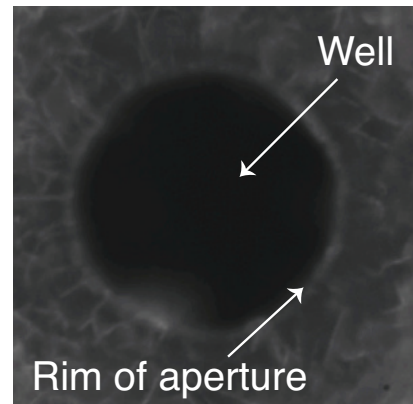


Fig. S20. Microscopy image of a Meca 4-chip cavity with 50 μm diameter on which a lipid bilayer will be formed. As the image shows, the rim of aperture where the film is anchored displays small irregularities, which are different from well to well, contributing to the variations in the quality of the anchored films and corresponding signals.

247

248 **References**

- 249 1. VR Ardham, V Zoni, S Adamowicz, P Campomanes, S Vanni, Accurate estimation of membrane capacitance from
250 atomistic molecular dynamics simulations of zwitterionic lipid bilayers. *The J. Phys. Chem. B* **124**, 8278–8286 (2020).
- 251 2. Z Vasilkoski, AT Esser, T Gowrishankar, JC Weaver, Membrane electroporation: The absolute rate equation and
252 nanosecond time scale pore creation. *Phys. review E* **74**, 021904 (2006).
- 253 3. A Barnett, JC Weaver, Electroporation: a unified, quantitative theory of reversible electrical breakdown and mechanical
254 rupture in artificial planar bilayer membranes. *Bioelectrochemistry bioenergetics* **25**, 163–182 (1991).
- 255 4. I Abidor, et al., Electric breakdown of bilayer lipid membranes: I. the main experimental facts and their qualitative
256 discussion. *J. electroanalytical chemistry interfacial electrochemistry* **104**, 37–52 (1979).
- 257 5. M Garten, et al., Whole-guv patch-clamping. *Proc. Natl. Acad. Sci.* **114**, 328–333 (2017).
- 258 6. PJ Beltramo, L Scheidegger, J Vermant, Toward realistic large-area cell membrane mimics: excluding oil, controlling
259 composition, and including ion channels. *Langmuir* **34**, 5880–5888 (2018).
- 260 7. V Vitkova, D Mitkova, K Antonova, G Popkirov, R Dimova, Sucrose solutions alter the electric capacitance and dielectric
261 permittivity of lipid bilayers. *Colloids surfaces A: physicochemical engineering aspects* **557**, 51–57 (2018).
- 262 8. LC Gross, AJ Heron, SC Baca, MI Wallace, Determining membrane capacitance by dynamic control of droplet interface
263 bilayer area. *Langmuir* **27**, 14335–14342 (2011).
- 264 9. N Kučerka, S Tristram-Nagle, JF Nagle, Structure of fully hydrated fluid phase lipid bilayers with monounsaturated
265 chains. *The J. membrane biology* **208**, 193–202 (2006).
- 266 10. NA Corvalán, AF Caviglia, I Felsztyna, R Itri, R Lascano, Lipid hydroperoxidation effect on the dynamical evolution of
267 the conductance process in bilayer lipid membranes: a condition toward criticality. *Langmuir* **36**, 8883–8893 (2020).
- 268 11. G Weber, et al., Lipid oxidation induces structural changes in biomimetic membranes. *Soft Matter* **10**, 4241–7 (2014).
- 269 12. Y Guo, VA Baulin, F Thalmann, Peroxidised phospholipid bilayers: insight from coarse-grained molecular dynamics
270 simulations. *Soft matter* **12**, 263–271 (2016).
- 271 13. H Junqueira, et al., Molecular organization in hydroperoxidized popc bilayers. *Biochimica et Biophys. Acta (BBA)-*
272 *Biomembranes* **1863**, 183659 (2021).
- 273 14. G Scanavachi, et al., Lipid hydroperoxide compromises the membrane structure organization and softens bending rigidity.
274 *Langmuir* **37**, 9952–9963 (2021).
- 275 15. T Kotnik, L Rems, M Tarek, D Miklavčič, Membrane electroporation and electropermeabilization: mechanisms and
276 models. *Annu. review biophysics* **48**, 63–91 (2019).
- 277 16. F Pein, A Bartsch, C Steinem, A Munk, Heterogeneous idealization of ion channel recordings—open channel noise. *IEEE*
278 *Transactions on NanoBioscience* **20**, 57–78 (2020).
- 279 17. A VanDongen, A new algorithm for idealizing single ion channel data containing multiple unknown conductance levels.
280 *Biophys. J.* **70**, 1303–1315 (1996).
- 281 18. RB Lira, FS Leomil, RJ Melo, KA Riske, R Dimova, To close or to collapse: the role of charges on membrane stability
282 upon pore formation. *Adv. Sci.* **8**, 2004068 (2021).
- 283 19. SW Kowalczyk, AY Grosberg, Y Rabin, C Dekker, Modeling the conductance and dna blockade of solid-state nanopores.
284 *Nanotechnology* **22**, 315101 (2011).
- 285 20. N Momin, et al., Designing lipids for selective partitioning into liquid ordered membrane domains. *Soft Matter* **11**, 3241–50
286 (2015).